



2 DOCTORAL THESIS

4 Optimisation studies and background
5 estimation in searches for the supersymmetric
6 partner of the top quark in all-hadronic final
7 states with the ATLAS Detector at the LHC

9 *A thesis submitted in fulfillment of the requirements
10 for the degree of Doctor of Philosophy*

11 *in the*

12 Experimental Particle Physics Research Group
13 School of Mathematical and Physical Sciences

14 *Author:*
14 Fabrizio MIANO

Supervisor:
Dr. Fabrizio SALVATORE

15 12th December 2017

Dedicated to my family.

*Have no fear for atomic energy
'cause none of them can stop the
time*

17

Robert Nesta Marley

18

Acknowledgments

- ¹⁹ Thanks to every single thing that went wrong. It made me stronger.

Declaration

21 I, Fabrizio MIANO, hereby declare that this thesis, titled, "Optimisation studies and back-
22 ground estimation in searches for the supersymmetric partner of the top quark in all-
23 hadronic final states with the ATLAS Detector at the LHC" has not been and will not be,
24 submitted in whole or in part to another University for the award of any other degree.

25 *Brighton, 12th December 2017*

University of Sussex
School of Mathematical and Physical Sciences
Experimental Particle Physics Research Group

Doctoral Thesis

31
32 Optimisation studies and background estimation in searches for
33 the supersymmetric partner of the top quark in all-hadronic final
34 states with the ATLAS Detector at the LHC

36 by Fabrizio MIANO

Abstract

This thesis presents searches for supersymmetry in $\sqrt{s} = 13$ TeV proton-proton collisions at the LHC using data collected by the ATLAS detector in 2015, 2016 and 2017. Events with 4 or more jets and missing transverse energy were selected. Kinematic variables were investigated and optimisations were performed to increase the sensitivity to supersymmetric signals. Standard Model backgrounds were estimated by means of Monte Carlo simulations and data-driven techniques. Before analysing the data in the blinded signal regions the agreement between data and background predictions and the extrapolations from control and validation regions to signal regions were validated. The analysis yielded no significant excess in any of the analyses performed. Therefore limits were set and the results were interpreted as lower bounds on the masses of supersymmetric particles in various scenarios and models.

49 **Contents**

50	Introduction	1
51	1 The Standard Model of particle physics and Supersymmetry	2
52	1.1 The Standard Model	2
53	1.1.1 Electroweak Symmetry Breaking and the Higgs mechanism	6
54	1.1.2 Limitations of the Standard Model	8
55	1.2 Supersymmetry	10
56	1.2.1 Why SUSY?	11
57	1.2.2 Minimal Supersymmetric Standard Model	12
58	1.2.3 Phenomenology of Supersymmetry	14
59	2 The ATLAS Experiment at the LHC	19
60	2.1 The LHC	19
61	2.2 The ATLAS Detector	21
62	2.2.1 The Magnet System	23
63	2.2.2 The Inner Detector	24
64	2.2.3 The Calorimeters	26
65	2.2.4 The Muon Spectrometer	28
66	2.3 The ATLAS Trigger System	29
67	3 The ATLAS Trigger System	30
68	3.1 Overview	30
69	3.2 Level-1 Trigger	31
70	3.2.1 The CTP	32
71	3.2.2 The L1 Calorimeter Trigger	32
72	3.2.3 The L1 Muon Trigger	33
73	3.3 High-Level Trigger	34
74	3.3.1 Inner detector tracking	35
75	3.3.2 Performance of HLT	35
76	4 Event Simulation and Reconstruction	41
77	4.1 Event Simulation	41

78	4.1.1 Event Generation	41
79	4.1.2 Detector Simulation	41
80	4.2 Object Reconstruction	41
81	4.2.1 Tracks and vertices	41
82	4.2.2 Electrons	42
83	4.2.3 Muons	42
84	4.2.4 Jets	42
85	4.2.5 Missing Transverse Energy	42
86	4.2.6 Overlap Removal	42
87	5 Stop searches in final states with jets and missing transverse energy	43
88	6 Results and Statistical Interpretations	44
89	Appendix A	45
90	Bibliography	46

⁹¹ List of Tables

⁹²	1.1 Forces and mediators described by the SM	6
⁹³	1.2 SUSY particles in the MSSM	13
⁹⁴	1.3 Parameters in the pMSSM.	15

List of Figures

96	1.1 The elementary particles of the Standard Model. From the outermost to the innermost; fermions (quarks, top-half wheel, leptons, bottom-half wheel), vector bosons, and the Higgs boson.	3
97	1.2 The Higgs potential in the complex plane.	8
100	1.3 Summary of several Standard Model total production cross-section measurements, corrected for leptonic branching fractions, compared to the corresponding theoretical expectations. All theoretical expectations were calculated at NLO or higher. The luminosity used for each measurement is indicated close to the data point. Uncertainties for the theoretical predictions are quoted from the original ATLAS papers. They were not always evaluated using the same prescriptions for PDFs and scales. Not all measurements are statistically significant yet [1].	9
101		
102		
103		
104		
105		
106		
107		
108	1.4 One-loop quantum corrections to the Higgs mass. A fermion correction with coupling λ_f	10
109		
110		
111		
112		
113		
114		
115		
116	1.5 The inverse couplings of electromagnetic (dashed blue), weak (dashed red) and strong (solid green) interactions with the SM (left) and a supersymmetric model (right). In the SM the three lines do not meet at one point, but with the introduction of supersymmetry, and assuming that the supersymmetric particles are not heavier than about 1 TeV, they do meet. This is an indication that supersymmetry could be discovered at the LHC.	11
117		
118		
119		
120		
121	1.6 NLO+NLL production cross-sections as a function of mass at $\sqrt{s} = 13\text{TeV}$ [2]	16
122		
123	1.7 Illustration of stop decay modes in the $(m_{\tilde{t}_1}, m_{\tilde{\chi}_1^0})$ mass place where the $\tilde{\chi}_1^0$ is assumed to be the lightest supersymmetric particle. The dashed blue lines indicate thresholds separating regions where different processes dominate.	17
121	1.8 Diagrams of the decay topologies of the signal models considered in this work. The term "soft" refers to decay products that have transverse momenta below the detector thresholds.	18
122		
123		

124	2.1 CERN Accelerator complex. The LHC is the last ring (dark grey line). Smaller machines are used for early-stage acceleration and also to provide beams for other experiments [3].	21
125		
126		
127	2.2 Cut-away view of the ATLAS detector. The dimensions of the detector are 25 m in height and 44 m in length. The overall weight of the detector is approximately 7000 tonnes [3].	22
128		
129		
130	2.3 The ATLAS magnet system.	23
131		
132	2.4 The ATLAS Inner Detector	24
133		
134	2.5 A computer generated image of the full calorimeter.	27
135		
136	2.6 Cut-away view of the ATLAS muon system [4].	28
137		
138		
139		
140	3.1 The ATLAS TDAQ system. L1Topo and FTK [5] have not been used for the results shown in this thesis.	31
141		
142		
143	3.2 An Electron-trigger chain (from [6]).	32
144		
145		
146	3.3 Illustration of the electron/photon and tau algorithms with the sums to be compared to programmable thresholds (from [6]).	33
147		
148		
149		
150	3.4 A schematic view of the L1 muon trigger chambers (from [6]).	34
151		
152	3.5 The ID tracking efficiency for the 24 GeV electron trigger is shown as a function of the (a) η and (b) p_T of the track of the offline electron candidate. Uncertainties based on Bayesian statistics are shown (from [5]).	36
153		
154		
155		
156	3.6 The ID tracking performance for the 6 GeV muon trigger; (a) efficiency as a function of the offline reconstructed muon p_T , (b) the resolution of the transverse impact parameter, d_0 as a function of the offline reconstructed muon p_T . Uncertainties based on Bayesian statistics are shown (from [5]).	37
157		
158	3.7 An illustration of the RoIs from the single-stage and two-stage tau lepton trigger tracking, shown in plan view (x-z plane) along the transverse direc- tion and in perspective view. The z-axis is along the beam line. The combined tracking volume of the 1 st and 2 nd stage ROI in the two-stage tracking approach is significantly smaller than the ROI in the one-stage tracking scheme (from [5]).	38
159		
160		
161		
162	3.8 The trigger performance for primary vertices in the b -jet signatures for 55, 110 and 260 GeV jet triggers; (a) the vertexing efficiency as a function of the number of offline tracks within the jets used for the vertex tracking, (b) the resolution in z of the vertex with respect to the offline vertex position as a function of the number of offline tracks from the offline vertex (from [5]). .	38
163		

- 3.9 Turn-on curves of various E_T^{miss} triggers: Figure 3.9a shows the efficiency as a function of offline E_T^{miss} for three different E_T^{miss} trigger algorithms. Three different E_T^{miss} high-level trigger algorithms are shown: HLT_xe80_tc_lcw_L1XE50 calculates E_T^{miss} based on calibrated clusters of calorimeter cells, and has a nominal threshold of 80 GeV. HLT_xe90_mht_L1XE50 calculates E_T^{miss} based on reconstructed jets, and has a nominal threshold of 90 GeV. HLT_xe100_L1XE50 calculates E_T^{miss} based on calorimeter cells calibrated at the electromagnetic scale, and has a nominal threshold (at the electromagnetic scale) of 100 GeV. All three algorithms are seeded by a Level-1 trigger algorithm with a nominal threshold of 50 GeV which is also shown; Figure 3.9b shows missing transverse energy trigger efficiencies for HLT_xe110_pufit_L1XE50 and HLT_xe110_mht_L1XE50 and for the corresponding L1 seed (L1_XE50). (from [7]).

¹⁷¹ Introduction

¹⁷² Last thing to write

¹⁷³ **1** | ¹⁷⁴ **The Standard Model of particle physics and Supersymmetry**

¹⁷⁵

A theory is something nobody believes, except the person who made it. An experiment is something everybody believes, except the person who made it.

Albert Einstein

¹⁷⁶ In this chapter, an overview of the Standard Model (SM) of particle physics will be
¹⁷⁷ presented in Section 1.1 together with its limitations in Section 1.1.2 and the need of an
¹⁷⁸ extension. One of the most popular, supersymmetry, will be discussed in Section 1.2
¹⁷⁹ where, an overview of the theory, together with the motivations behind its success, will
¹⁸⁰ be presented in Section 1.2.1, followed by the description of the Minimal Supersymmetric
¹⁸¹ Standard Model (MSSM) in Section 1.2.2, and finally, the phenomenology of super-
¹⁸² symmetry, with particular attention on third-generation supersymmetry, as it is the most
¹⁸³ relevant theoretical support to the analyses presented in this work, will be discussed in
¹⁸⁴ Section 1.2.3.

¹⁸⁵ **1.1 The Standard Model**

¹⁸⁶ The SM is an effective theory that aims to provide a general description of fundamental
¹⁸⁷ particles and their interactions. Unfortunately, our understanding of nature is still limited
¹⁸⁸ due to some opened question the SM is not able to answer to.

¹⁸⁹ The 20th century can be considered a quantum revolution. Several experiments led to
¹⁹⁰ discoveries which were found to be, together with the formalised theory, a solid base of
¹⁹¹ the Standard Model of particle physics and our description of nature. Several particles
¹⁹² were first predicted and then experimentally observed e. g. the W and the Z bosons, the
¹⁹³ τ lepton, [8], and more recently the Higgs boson at the LHC discovered by ATLAS [9]
¹⁹⁴ and CMS [10].

¹⁹⁵ The SM is a Quantum Field Theory (QFT) where particles are treated like excitations
¹⁹⁶ of quantum fields in a four-dimensional Minkowski spacetime. It can describe three of

197 the four fundamental forces; weak, electromagnetic, and strong, but not gravity.

198 The most general classification of the
 199 elementary particles within the SM can
 200 be made by means of spin and their be-
 201 haviour under Poincaré transformations:
 202 *fermions* (leptons and quarks), usually re-
 203 ferred to as matter, which have half-
 204 integer spin values, in unit of \hbar , and *bo-*
 205 *s**ns*, usually referred to as information
 206 carriers, which have integer-spin values.
 207 A noteworthy subset of bosons is formed
 208 by the Spin-1 bosons, also known as gauge
 209 bosons. These can be considered medi-
 210 ators of the forces. Figure 1.1 displays
 211 the elementary particles of the Standard
 212 Model known as of today.

213 Symmetries and Gauge Groups

214 In 1915, the German mathematician and
 215 theoretical physicist Emmy Noether (23
 216 March 1882 – 14 April 1935) proved that
 217 every differentiable symmetry of the action - defined as the integral over space of a Lag-
 218 rangian density function $S = \int \mathcal{L} dt$ - of a physical system has a corresponding conser-
 219 vation law. More generally, a symmetry is a property of a physical system and under
 220 certain transformations this property is preserved.

221 A gauge theory in QFT, is a theory in which the Lagrangian is invariant under a con-
 222 tinuous group of local transformations. Group theory was adopted to describe the sym-
 223 metries conserved in the SM. The gauge group of the SM is the *Lie Group* which contains
 224 all the transformations between possible gauges. The Lie algebra of group generators is
 225 associated to any Lie group and for each group generator there emerges a corresponding
 226 field, called the gauge field, and the quanta of such fields are called *gauge bosons*.

227 The three SM interactions can therefore be mathematically described by the following:

$$U(1)_Y \otimes SU(2)_L \otimes SU(3)_C \quad (1.1)$$

228 Here, Y is the weak hypercharge, used to estimate the correlation between the electric
 229 charge (Q) and the third component of the weak isospin (I_3) via the relation $Q = I_3 + Y/2$,
 230 where I_3 can either be $\pm 1/2$ or 0 for left-handed and right-handed particles, respectively;
 231 C the colour charge and L the left-handedness.

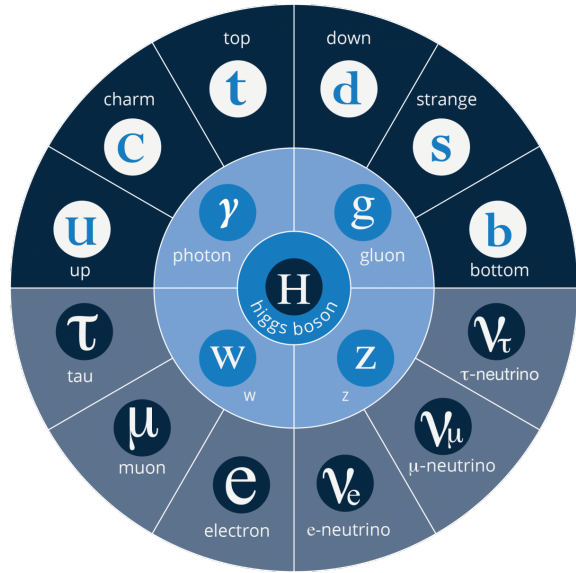


Figure 1.1: The elementary particles of the Standard Model. From the outermost to the innermost; fermions (quarks, top-half wheel, leptons, bottom-half wheel), vector bosons, and the Higgs boson.

232 QED is an Abelian gauge theory described by the symmetry group $U(1)$. The elec-
233 tromagnetic four-potential is its gauge field and the photon its gauge boson [11]. The
234 interactions between charged fermions occurs by the exchange of a massless photon.

235 The weak interaction is described by the non-Abelian gauge group $SU(2)$. The $SU(2)$
236 generators are the massless gauge bosons $W_\mu^{\alpha=1,\dots,3}$ and they violate the parity by acting
237 only on left-handed particles. As a consequence of non-Abelianity, $SU(2)$ gauge bosons
238 can self-interact as the generator commutators are non-vanishing. Additionally, quarks
239 can also interact through weak interaction as mixtures of SM eigenstates as described by
240 the CKM matrix [12].

241 Finally, the strong interaction, described by the symmetry group $SU(3)$, has eight
242 massless gauge bosons, the gluons, $G_\mu^{\alpha=1,\dots,8}$ which can be exchanged between quarks
243 and can also self-interact.

244 Fermions

245 There are twelve fermions in the SM: six quarks and six leptons. In particular, fermions
246 can be grouped into three generations. Each generation contains four particles; one up-
247 and one down-type quark, one charged lepton and one neutral lepton. The masses of the
248 charged leptons and quarks increase with the generation. The six quarks of the SM can
249 be grouped into three $S(2)$ doublets;

$$\begin{pmatrix} u \\ d \end{pmatrix}, \quad \begin{pmatrix} c \\ s \end{pmatrix}, \quad \begin{pmatrix} t \\ b \end{pmatrix}$$

250 The up-type quarks (*up, charm, top*) have charge $+\frac{2}{3}e$ and the down-type quarks (*down,*
251 *strange, beauty/bottom*) have charge $-\frac{1}{3}e$, where e is the electron charge. Quarks also have
252 another quantum number that can be seen as the analogue of the electric charge; the col-
253 our charge. This can exist in three different states; *red, green* and *blue*, but they cannot
254 exist as free particles. They rather group to form hadronic matter, also known as *had-*
255 *rons*. There are two kinds of hadrons; mesons and baryons. Mesons are quark-antiquark
256 systems, e.g. the pion, and baryons are three-quark system, e.g. protons and neutrons.
257 Quarks and anti-quarks have a baryon number of $\frac{1}{3}$ and $-\frac{1}{3}$, respectively.

258 There are six leptons and they can be classified in charged leptons (electron e , muon
259 μ , tau τ) and neutral leptons (electron neutrino ν_e , muon neutrino ν_μ , tau neutrino ν_τ).

$$\begin{pmatrix} \nu_e \\ e^- \end{pmatrix}, \quad \begin{pmatrix} \nu_\mu \\ \mu^- \end{pmatrix}, \quad \begin{pmatrix} \nu_\tau \\ \tau^- \end{pmatrix}$$

260 Each lepton has a characteristic quantum number, called lepton number (L). Negat-
261 ively (positively) charged leptons have $L = -1$ ($L = 1$) and neutral leptons have $L = 1$.
262 The lepton number is conserved in all the interactions.

263 **Forces of Nature**

264 Forces in the SM are described by gauge theories, where the interactions are mediated by
 265 a vector gauge boson.

266 The electromagnetic force is described by Quantum Electrodynamics (QED) and, as
 267 its mediator is the photon (γ) which couples to charged particles, it only affects charged
 268 leptons and quarks, not neutrinos which are instead affected by the weak force, mediated
 269 by the W^\pm and Z^0 bosons.

270 The weak interaction is associated with handedness (the projection of a particle spin
 271 onto its direction of motion). Both leptons and quarks have left- and right-handed com-
 272 ponents. However, only the left-handed (right-handed) component for neutrinos (anti-
 273 neutrinos) has been observed. This means that nature prefers to produce left-handed
 274 neutrinos and right-handed anti-neutrinos, which is the so-called *parity violation*.

275 The strong interaction, mediated by the gluon, electrically neutral and massless, is de-
 276 scribed by Quantum ChromoDynamics (QCD). Its coupling (α_s) increases with increas-
 277 ing distance and is smaller at short range. In particular, α_s evolves as a function of the
 278 transferred four-momentum squared, Q^2 , as follows:

$$\alpha_s(Q^2) \propto \frac{1}{n_f \log\left(\frac{Q^2}{\Lambda_{\text{QCD}}^2}\right)} \quad (1.2)$$

279 where n_f is the number of quarks with mass below Q^2 and Λ_{QCD} is the QCD character-
 280 istic scale, so Eq. 1.2 shows that α_s decreases as a function of Λ_{QCD} , but at the same time
 281 it quickly diverges when Q^2 gets closer to Λ . In other words, as the condition $\alpha_s \ell^+ \ell^- 1$
 282 only holds for $Q^2 \gg \Lambda_{\text{QCD}}$, QCD can be treated perturbatively only at high energy scales.

283 Moreover, three facts arise;

284 • *confinement*: quarks or gluons cannot be observed as free particles, but only col-
 285 ourless “singlet” states can be observed as “jets”, namely collimated cone-shaped
 286 sprays of hadrons;

287 • *asymptotic freedom*: interactions between quarks and gluons become weaker as the
 288 energy scale increases and the corresponding length scale decreases, as $\alpha_s \rightarrow 0$ for
 289 $Q^2 \rightarrow \infty$;

290 • *hadronisation*: when quarks or gluons are pulled apart, the production of pairs of
 291 hadrons, produced from the vacuum, is energetically preferred to an increase in
 292 distance.

293 Table 1.1 summarises the forces described in the SM and the main characteristics of
 294 the mediators. The gravitational force is believed to be mediated by the graviton, but as
 295 already mentioned, since it is not included in the SM, it will not be further discussed.

Table 1.1: Forces and mediators described by the SM

Force	Name	Symbol	Mass [GeV]	Charge
Electromagnetic	Photon	γ	0	0
Weak	W	W^\pm	80.398	$\pm e$
	Z	Z^0	91.188	0
Strong	Gluon	g	0	0

296 1.1.1 Electroweak Symmetry Breaking and the Higgs mechanism

297 In 1979 Sheldon Glashow, Abdus Salam, and Steven Weinberg were awarded the Nobel
 298 Prize in Physics for their contributions to the so-called electroweak unification. In the
 299 mathematical description of the SM in 1.1, the electroweak interaction is described by
 300 $U(1)_Y \otimes SU(2)_L$.

301 The four electroweak physical bosons W^\pm , Z and γ are related to the four unphysical
 302 gauge bosons $W_\mu^{\alpha=1,\dots,3}$ and B_μ . In particular, to obtain the physical bosons the gauge
 303 bosons have to mix as follows;

$$A_\mu = W_\mu^3 \sin \theta_W + B_\mu \cos \theta_W \quad (1.3)$$

304

$$Z_\mu = W_\mu^3 \cos \theta_W - B_\mu \sin \theta_W \quad (1.4)$$

305

$$W_\mu^\pm = \frac{1}{\sqrt{2}} (W_\mu^1 \mp i W_\mu^2) \quad (1.5)$$

306 Here, θ_W is the so-called *Weinberg angle* which is the angle by which spontaneous sym-
 307 metry breaking rotates the original gauge bosons W_μ^3 and B_μ into the physical Z and γ .
 308 A_μ and Z_μ are the photon and the Z boson fields, respectively. The θ_W angle can be ex-
 309 perimentally determined in terms of the coupling strengths, of the $B_\mu(g_1)$ and the $W_\mu^\alpha(g_2)$
 310 to the fermions, using the relation $\tan \theta_W = g_1/g_2$. The field mixing of gauge bosons that
 311 gives birth to the physical ones can be mathematically expressed by the following:

312 The mass terms for both gauge bosons and fermionic fields are forbidden by the elec-
 313 troweak gauge as they are not invariant under gauge transformations. Nonetheless, it
 314 was experimentally proven that W and Z bosons are massive [11], therefore in order for
 315 the SM assumption to hold, the electroweak symmetry must be broken.

316 The SM Lagrangian can be written as the sum of the various Lagrangians describing
 317 the three interactions and the masses of the elementary particles as follows:

$$\mathcal{L}_{\text{SM}} = \mathcal{L}_{\text{EWK}} + \mathcal{L}_{\text{QCD}} + \mathcal{L}_{\text{Mass}} \quad (1.6)$$

318 In order for the SM Lagrangian to remain a renormalisable theory, the mass terms ($\mathcal{L}_{\text{Mass}}$)
 319 cannot be insterted by hand. A mechanism, that can preserve the gauge symmetry in the

320 SM and can solve the inconsistency arisen from the mass difference between the gauge
 321 bosons and the physical ones, is needed. A British theoretical physicist, Peter Higgs (29
 322 May 1929, Newcastle upon Tyne, UK), came up with a brilliant solution for which he was
 323 awarded the Nobel Prize in Physics in 2013. Higgs proposed that broken symmetry in
 324 the electroweak theory could explain the origin of masses of elementary particles, and in
 325 particular of W and Z bosons. The mechanism introduces a scalar field, known as the
 326 Higgs field, thought to couple to both massive fermions and bosons. The $SU(2)$ doublet
 327 is then introduced in the SM;

$$\phi = \begin{pmatrix} \phi^+ \\ \phi^0 \end{pmatrix} \quad (1.7)$$

328 with ϕ^+ and ϕ^0 generic complex fields:

$$\phi^+ = \frac{\phi_1 + i\phi_2}{\sqrt{2}}, \quad \phi^0 = \frac{\phi_3 + i\phi_4}{\sqrt{2}} \quad (1.8)$$

329 Consider a Lagrangian of the form:

$$\mathcal{L}_{\text{Higgs}} = (\partial_\mu \phi)^* (\partial^\mu \phi) - V(\phi) \quad (1.9)$$

330 Renormalizability and $SU(2)_L \otimes U(1)_Y$ invariance require the Higgs potential to be of the
 331 following form:

$$V(\phi) = \mu^2 \phi^\dagger \phi + \lambda \left(\phi^\dagger \phi \right)^2 \quad (1.10)$$

332 The Lagrangian in Eq. 1.9 is the Higgs Lagrangian if ϕ is chosen to be the following:

$$\phi = \begin{pmatrix} \phi^+ \\ \phi^0 \end{pmatrix} = \begin{pmatrix} G^+ \\ \frac{1}{\sqrt{2}}(v + H + iG^0) \end{pmatrix}$$

333 Here, the complex scalar field G^\pm and the real scalar field G^0 correspond to Goldstone
 334 bosons, and the real scalar field H is the SM Higgs boson field [13]. These massless scalars
 335 are absorbed due to the gauge transformations by the electroweak gauge bosons of the
 336 SM:

$$\phi = \begin{pmatrix} \phi^+ \\ \phi^0 \end{pmatrix} = \begin{pmatrix} 0 \\ \frac{1}{\sqrt{2}}(v + H) \end{pmatrix} \quad (1.11)$$

337 The Higgs potential in Eq. 1.10 is displayed in Fig. 1.2 if λ and μ are chosen to be real.
 338 Such potential has a non-zero ground state, v , also known as *vacuum expectation value*
 339 (VEV):

$$\phi_0 = \begin{pmatrix} 0 \\ \frac{1}{\sqrt{2}}v \end{pmatrix} \quad (1.12)$$

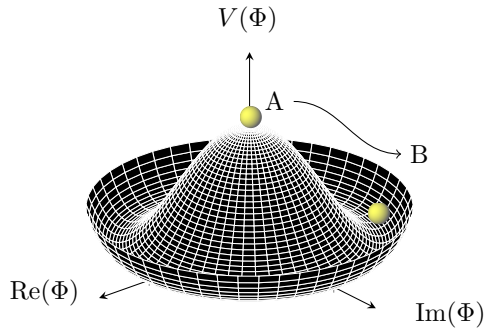


Figure 1.2: The Higgs potential in the complex plane.

340 Such representation remains invariant under $U(1)$ allowing electric charge conservation.
 341 However, the SM gauge symmetry 1.1 is broken into $SU(2)_L \otimes U(1)_Y$.
 342 In summary, to generate particle masses gauge symmetry must be broken. How-
 343 ever, in order for the theory to remain renormalisable, the global Lagrangian symmetry
 344 must be preserved. This can be solved introducing the concept of *spontaneous* symmetry
 345 breaking (SSB): a mechanism that allows a symmetric Lagrangian, but not a symmet-
 346 ric vacuum. In particular, given a Lagrangian invariant under a certain transformation,
 347 T_X , and a generic set of states, that transform under T_X as the elements of a multiplet,
 348 the symmetry is spontaneously broken if one of those states is arbitrarily chosen as the
 349 ground state of the system. The interaction of the Higgs field with the $SU(2) \otimes U(1)$
 350 gauge fields, $W_\mu^{\alpha=1,2,3}$, result in the three gauge bosons fields acquiring mass whilst the
 351 A_μ field remains massless.

352 1.1.2 Limitations of the Standard Model

353 During Run 1 and 2 of the LHC, the SM has been extensively validated, as shown in
 354 Fig. 1.3: the agreement, between the measured production cross-section of various SM
 355 processes and the SM predictions, looks very good. However, there are some funda-
 356 mental questions that have still no answer.

357 Hierarchy Problem

358 Due to the coupling of the Higgs field to the fermionic fields the one-loop corrections to
 359 the Higgs mass receive several contributions. In particular, looking at Fig. 1.4:

$$\Delta m_H^2 = -\frac{|\lambda_f|^2}{8\pi^2} \Lambda_{UV}^2 + \dots \quad (1.13)$$

360 where, λ_f is the coupling constant to the fermionic field; Δm_H^2 is the difference between
 361 the observed Higgs mass m_H^2 and the bare mass, m_H^0 (Lagrangian parameter); Λ_{UV} is
 362 the ultraviolet momentum cut-off, selected to be at the Planck scale ($\sim 2 \cdot 10^{18}$ GeV), at
 363 which a QFT description of gravity is believed to become possible. The correction to the

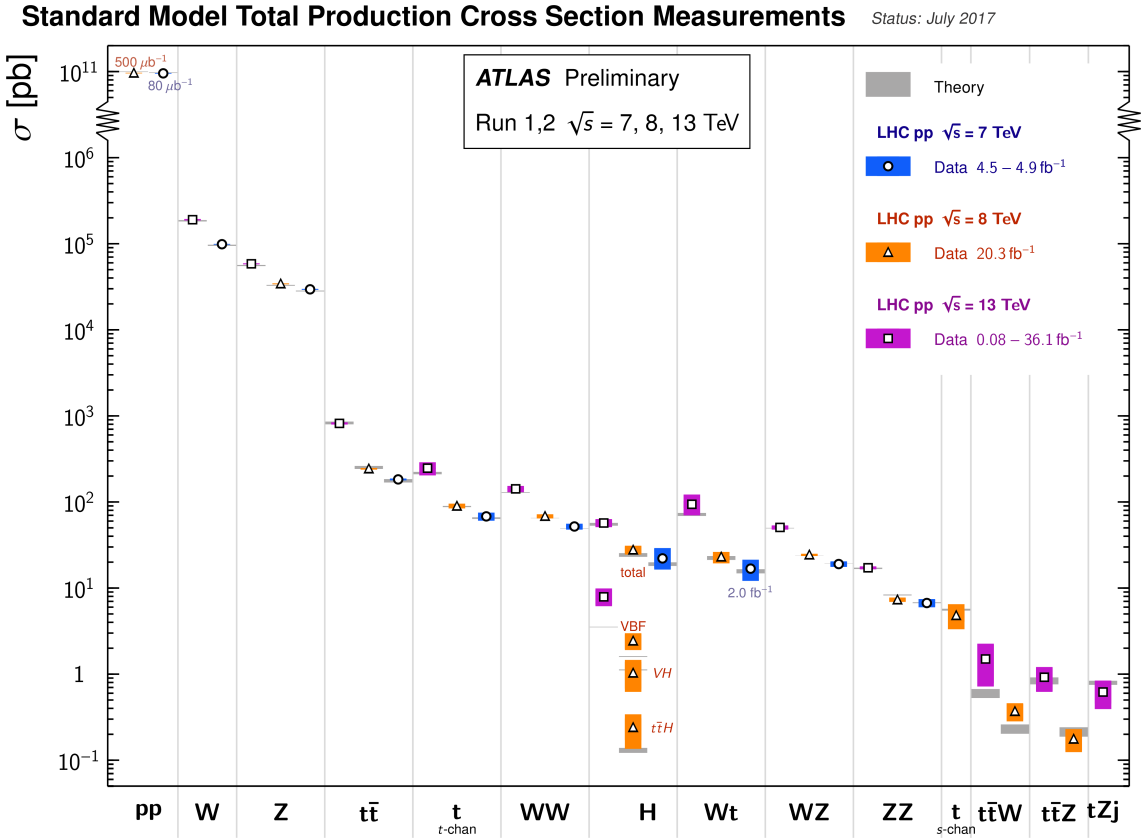


Figure 1.3: Summary of several Standard Model total production cross-section measurements, corrected for leptonic branching fractions, compared to the corresponding theoretical expectations. All theoretical expectations were calculated at NLO or higher. The luminosity used for each measurement is indicated close to the data point. Uncertainties for the theoretical predictions are quoted from the original ATLAS papers. They were not always evaluated using the same prescriptions for PDFs and scales. Not all measurements are statistically significant yet [1].

Higgs mass then, will be around 30 orders of magnitude larger than Higgs mass itself, in opposition to what has been measured. This difference just mentioned, between the electroweak scale and the Planck scale arisen from the quantum corrections to the Higgs mass, is the so-called Hierarchy Problem [14].

368 Neutrino Masses

The Super-Kamiokande Collaboration first, in 1998 [15], and SNO Collaboration later, in 2001 [16], have provided measurements of the neutrino flux from solar and atmospheric sources. The Nobel Prize in Physics 2015 was awarded jointly to Takaaki Kajita and Arthur B. McDonald “for the discovery of neutrino oscillations, which shows that neutrinos have mass” [17]. Such feature contradicts the presence of the neutrinos in the SM which are assumed to be massless.

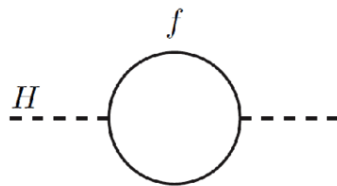


Figure 1.4: One-loop quantum corrections to the Higgs mass. A fermion correction with coupling λ_f .

³⁷⁵ Dark Matter

³⁷⁶ Although dark matter (DM) has never been directly observed, its existence is inferred
³⁷⁷ from its gravitational effects. For example, looking at galaxies rotation, it was observed
³⁷⁸ that the rotation speed was higher than expected, given the amount of visible matter.
³⁷⁹ Two different reasoning arose during the last century to justify such effect: there is either
³⁸⁰ matter that cannot be seen by us (in terms of visible light), which contributes to the gal-
³⁸¹ atcis mass, or the general relativity works differently at galactic distances. The former is
³⁸² believed to be the most likely and it implies the existence of new particles which do not in-
³⁸³ teract via electromagnetic interaction, the so-called Weakly Interacting Massive Particles
³⁸⁴ (WIMPs).

³⁸⁵ 1.2 Supersymmetry

³⁸⁶ Supersymmetry, also known as SUSY, introduces a space-time symmetry that relates bo-
³⁸⁷ sons to fermions and vice-versa, via a transformation of the form:

$$Q |\text{fermion}\rangle = |\text{boson}\rangle, \quad Q |\text{boson}\rangle = |\text{fermion}\rangle \quad (1.14)$$

³⁸⁸ For each SM particle there exists a supersymmetric partner, generally called *sparticle*
³⁸⁹ (where the s stands for “scalar”), with a spin difference of $\Delta s = 1/2$. Each pair of part-
³⁹⁰ ners is arranged in a so-called *supermultiplet*. The two components have same masses
³⁹¹ and quantum numbers, but different spin. *Sleptons* and *squarks* gauge quantum num-
³⁹² bers are the same as their SM equivalent, namely for example, the superpartners of the
³⁹³ left-handed SM fermion components couple weakly, but the superpartners of the right-
³⁹⁴ handed SM fermion components do not. Furthermore, gauge supermultiplets contain a
³⁹⁵ vector boson and two spin- $\frac{1}{2}$ fermions. Spin-1 bosons are arranged in gauge multiplets,
³⁹⁶ and their superpartners, referred to as *gauginos*, are spin- $\frac{1}{2}$ fermions. Unlike the SM, the
³⁹⁷ Spin-0 Higgs boson has two supermultiplets containing sparticles with different weak
³⁹⁸ isospin values, referred to as H_u and H_d , which are required to give mass to both the up-
³⁹⁹ and down-type sparticles. Higgs SUSY partners are called the *Higgsinos*.

⁴⁰⁰ As of today, SUSY particles have not been observed, resulting in the assumption that
⁴⁰¹ SUSY must be a broken symmetry, otherwise superpartners would have the same masses
⁴⁰² as their SM equivalent. However, if sparticles were to be too heavy (close to the Planck

scale), the hierarchy problem would still remain unsolved. The soft SUSY breaking mechanism, described in Section 1.2.2, overcomes this problem by imposing constraints on the masses of sparticles to a range that can be experimentally explored.

1.2.1 Why SUSY?

One of the main motivations for SUSY is the cancellation of quadratic divergences to Δm_H^2 . The introduction of SUSY particles, with a half-integer spin difference with respect to their SM partners, provides a solution to the hierarchy problem. The Higgs mass squared potential receives corrections from a new scalar of mass of the form:

$$\Delta m_H^2 = -\frac{|\lambda_S|^2}{16\pi^2} \left[\Lambda_{UV}^2 - 2m_S^2 \ln(\Lambda_{UV}/m_S) + \dots \right] \quad (1.15)$$

where, λ_S is the coupling of SUSY particles to the Higgs field. This term cancels the fermionic contributions in Eq. 1.13 since the couplings are the same. The experimental value of Higgs mass will then not need any fine tuning.

Furthermore, Fig. 1.5 shows the inverse couplings as a function of the scale for both SM and the Minimal Supersymmetric Standard Model (MSSM), which will be soon discussed. In the SM the three lines, representing electromagnetic (dashed blue), weak (dashed red) and strong (solid green) interactions respectively, do not meet at one point, but with the introduction of supersymmetry, and assuming that the supersymmetric particles are not heavier than about 1 TeV, they do meet. This is an indication that supersymmetry could be discovered at the LHC as well as another good motivation for SUSY searches given the possible unification of the coupling constants at the Planck scale.

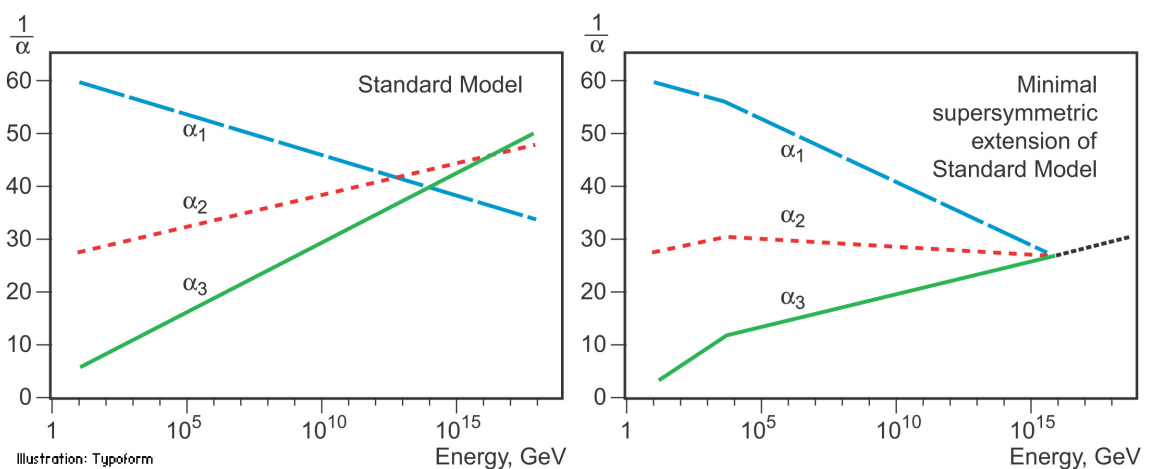


Figure 1.5: The inverse couplings of electromagnetic (dashed blue), weak (dashed red) and strong (solid green) interactions with the SM (left) and a supersymmetric model (right). In the SM the three lines do not meet at one point, but with the introduction of supersymmetry, and assuming that the supersymmetric particles are not heavier than about 1 TeV, they do meet. This is an indication that supersymmetry could be discovered at the LHC.

422 1.2.2 Minimal Supersymmetric Standard Model

423 There does not exist a unique extension of a supersymmetric Standard Model, i. e. SUSY
 424 is not a well-defined model but it is more a framework within which various SM exten-
 425 sions can be derived. The Minimal Supersymmetric Standard Model (MSSM), a minimal
 426 supersymmetric extension of the SM [18], is defined by essentially doubling up the num-
 427 ber of particles in the SM theory in order to include all the SM particles as well as their
 428 corresponding superpartners.

429 Soft SUSY breaking

430 The mass spectrum of the SUSY particles must sit somewhere at a larger scale than the SM
 431 one, as supersymmetric particles have not been discovered at the mass scale of their SM
 432 partners. This gives us a hint that supersymmetry cannot be an exact symmetry, there has
 433 to be an analogy with the electroweak symmetry breaking discussed in 1.1.1 that breaks
 434 SUSY. In particular, this must be soft or spontaneous such that broken supersymmetry
 435 still provides a solution to the hierarchy problem. This means that some new higher-
 436 energy-scale particles and interactions have to be added to the MSSM, but it also means
 437 that terms, containing only masses and couplings, with positive mass dimension, gauge
 438 invariant and violating SUSY, have to be added to the Lagrangian;

$$\mathcal{L}_{\text{MSSM}} = \mathcal{L}_{\text{SUSY}} + \mathcal{L}_{\text{soft}} \quad (1.16)$$

439 Here, $\mathcal{L}_{\text{SUSY}}$ contains the original SUSY invariant interaction and $\mathcal{L}_{\text{soft}}$ contains all the
 440 additional terms. A set of around 100 parameters - depending on the method - are then
 441 introduced into the theory.

442 A large amount of theoretical effort has been spent trying to understand the mech-
 443 anism for soft SUSY breaking in order to produce the desired superpartner masses and
 444 interactions properties. Among these three most studied mechanisms are;

- 445 • gravity-mediated supersymmetry breaking, also known as mSUGRA (minimal su-
 446 pergravity), which communicates supersymmetry breaking to the supersymmetric
 447 Standard Model through gravitational interactions [19];
- 448 • gauge-mediated supersymmetry breaking (GMSB) which communicates supersym-
 449 metry breaking to the supersymmetric Standard Model through the Standard Model's
 450 gauge interactions [20];
- 451 • anomaly-mediated supersymmetry breaking (AMSB), a special type of gravity-mediated
 452 supersymmetry breaking, that communicates supersymmetry breaking to the su-
 453 persymmetric Standard Model through the conformal anomaly [21, 22]

454 **MSSM mass spectrum**

455 As per the SM gauge bosons, the gaugino masses are affected by electroweak symmetry
 456 breaking. The new states, introduced in the $\mathcal{L}_{\text{soft}}$, mix to form the mass eigenstates of
 457 the sparticles. The neutral Winos, \tilde{W}^0 , Binos, \tilde{B}^0 and higgsinos \tilde{H}^0 mix to form the four
 458 *neutralinos* $\tilde{\chi}_i^0$ ($i = 1, 2, 3, 4$) as follows;

$$\begin{pmatrix} \tilde{\chi}_1^0 \\ \tilde{\chi}_2^0 \\ \tilde{\chi}_3^0 \\ \tilde{\chi}_4^0 \end{pmatrix} = \begin{pmatrix} M_1 & 0 & -c_\beta s_W m_Z & c_W s_\beta m_Z \\ 0 & M_2 & c_\beta c_W m_Z & -c_W s_\beta m_Z \\ -c_\beta s_W m_Z & c_\beta s_W m_Z & 0 & -\mu \\ s_\beta c_W m_Z & -s_\beta c_W m_Z & -\mu & 0 \end{pmatrix} \begin{pmatrix} \tilde{B}^0 \\ \tilde{W}^0 \\ \tilde{H}_u^0 \\ \tilde{H}_d^0 \end{pmatrix} \quad (1.17)$$

459 Here, $c_\beta = \cos \beta$, $(s_\beta) = \sin \beta$, $c_W = \cos \theta_W$ and $(s_W) = \sin \theta_W$. M_1, M_2 are related to
 460 gaugino masses and μ to higgsino mass, $\tan \beta$ is the ratio of the VEVs of the two Higgs
 461 doublet fields, θ_W is the ratio of the electroweak coupling constants and, m_Z (m_W) is the
 462 mass of the Z (W) boson. The neutralino indeces are conventionally assumed to increase
 463 with their masses. The charged winos \tilde{W}^\pm and higgsinos \tilde{H}^\pm mix to form four *charginos*,
 464 $\tilde{\chi}_i^\pm$ ($i = 1, 2$) as it follows;

$$\begin{pmatrix} \tilde{\chi}_1^\pm \\ \tilde{\chi}_2^\pm \end{pmatrix} = \begin{pmatrix} M_2 & \sqrt{2}m_W s_\beta \\ \sqrt{2}m_W c_\beta & \mu \end{pmatrix} \begin{pmatrix} \tilde{W}^\pm \\ \tilde{H}^\pm \end{pmatrix} \quad (1.18)$$

465 Charginos and neutralinos mix as described in Eq. 1.18 and 1.17 and will be referred
 466 to as bino-like, wino-like or higgsino-like depending on their phenomenology. Gluinos
 467 do not mix as they carry colour charge.

468 The Higgs sector is also affected. There are five mass eigenstates, h^0, H^0, A^0 , and H^\pm .
 469 These, together with the other MSSM particles are listed in Table 1.2.

Table 1.2: SUSY particles in the MSSM

Name	Spin	Gauge Eigenstates	Mass Eigenstates
Squarks (\tilde{q})	0	$\tilde{u}_L \tilde{u}_R \tilde{d}_L \tilde{d}_R$	(same)
		$\tilde{c}_L \tilde{c}_R \tilde{s}_L \tilde{s}_R$	(same)
		$\tilde{t}_L \tilde{t}_R \tilde{b}_L \tilde{b}_R$	$\tilde{t}_1 \tilde{t}_2 \tilde{b}_1 \tilde{b}_2$
Sleptons (\tilde{l})	0	$\tilde{e}_L \tilde{e}_R \tilde{\nu}_L$	(same)
		$\tilde{\mu}_L \tilde{\mu}_R \tilde{\nu}_L$	(same)
		$\tilde{\tau}_L \tilde{\tau}_R \tilde{\nu}_\tau$	$\tilde{\tau}_1 \tilde{\tau}_2 \tilde{\nu}_\tau$
Higgs bosons	0	$H_u^0 H_d^0 H_d^+ H_d^-$	$h^0 H^0 A^0 H^\pm$
Neutralinos ($\tilde{\chi}_j^0$)	1/2	$\tilde{B}^0 \tilde{W}^0 \tilde{H}_u^0 \tilde{H}_d^0$	$\tilde{\chi}_1^0 \tilde{\chi}_2^0 \tilde{\chi}_3^0 \tilde{\chi}_4^0$
Charginos ($\tilde{\chi}_i^\pm$)	1/2	$\tilde{W}^\pm \tilde{H}_u^+ \tilde{H}_u^-$	$\tilde{\chi}_1^\pm \tilde{\chi}_2^\pm$
Gluino	1/2	\tilde{g}	(same)
Gravitino	3/2	\tilde{G}	(same)

In the MSSM the squark sector is specified by the mass matrix in the basis $(\tilde{q}_L, \tilde{q}_R)$ with $\tilde{q} = \tilde{t}$ or \tilde{b} [23]. A rotation matrix can be defined also for left- and right-handed squarks and sleptons, although in the MSSM the mixing is assumed to be non-zero only for the third-generation scalar partners. Stop, \tilde{t}_L, \tilde{t}_R , sbottom \tilde{b}_L, \tilde{b}_R , and stau, $\tilde{\tau}_L, \tilde{\tau}_R$ rotate into mass eigenstates, $\tilde{t}_1, \tilde{t}_2, \tilde{b}_1, \tilde{b}_2, \tilde{\tau}_1, \tilde{\tau}_2$, respectively, as described in Eq. 1.19 [24].

$$\mathcal{M}_{\tilde{q}}^2 = \begin{pmatrix} m_{\tilde{q}_L}^2 & a_q m_q \\ a_q m_q & m_{\tilde{q}_R}^2 \end{pmatrix} \quad (1.19)$$

with

$$\begin{aligned} m_{\tilde{q}_L}^2 &= M_{\tilde{Q}}^2 + m_Z^2 \cos 2\beta \left(I_3^{q_L} - e_q \sin^2 \theta_W \right) + m_q^2, \\ m_{\tilde{q}_R}^2 &= M_{\{\tilde{U}, \tilde{D}\}}^2 + m_Z^2 \cos 2\beta e_q \sin^2 \theta_W + m_q^2, \\ a_q m_q &= \begin{cases} (A_t - \mu \cot \beta) m_t, & (\tilde{q} = \tilde{t}) \\ (A_b - \mu \tan \beta) m_t, & (\tilde{q} = \tilde{b}) \end{cases} \end{aligned} \quad (1.20)$$

Here, $I_3^{q_L}$ is the third component of the weak isospin and e_q the electric charge of the quark q . $M_{\{\tilde{Q}, \tilde{U}, \tilde{D}\}}$ and $A_{t,b}$ are soft SUSY-breaking parameters, μ is the higgsino mass parameter, and $\tan \beta$, as previously mentioned, is the ratio of Higgs field VEVs. By diagonalising the matrix in Eq. 1.19 one gets the mass eigenstates

$$\tilde{q}_1 = \tilde{q}_L \cos \theta_{\tilde{q}} + \tilde{q}_R \sin \theta_{\tilde{q}}$$

$$\tilde{q}_2 = -\tilde{q}_L \sin \theta_{\tilde{q}} + \tilde{q}_R \cos \theta_{\tilde{q}}$$

with the mass eigenvalues $m_{\tilde{q}_1}, m_{\tilde{q}_2}$ ($m_{\tilde{q}_1} < m_{\tilde{q}_2}$) and the mixing angle $\theta_{\tilde{q}}$ ($-\pi/2 < \theta_{\tilde{q}} \leq \pi/2$).

1.2.3 Phenomenology of Supersymmetry

As previously mentioned, the introduction of SUSY particles overcomes the problem of an unnatural fine-tuning to the Higgs mass due to its quadratic corrections.

R-parity

The most general MSSM can contain operators that violate baryon and/or lepton number, thus allowing proton decays. The non-observation of proton decays forbids the existence of such terms. A possibility to avoid these operators is to introduce a new discrete symmetry named *R*-parity. The conserved quantum number is defined as;

$$P_R = (-1)^{3(B-L)+2s} \quad (1.21)$$

where B, L , and s are the baryon, lepton, and spin number, respectively.

490 The SM particles have $R = 1$ and SUSY partners have $R = -1$. When R -parity
 491 conservation is imposed on MSSM models, the mixing between particles and sparticles
 492 cannot occur, resulting in the number of SUSY particles to be even at every interaction
 493 vertex. Furthermore, all sparticles must be pair-produced and the Lightest Supersym-
 494 metric Particle (LSP) has to be stable and can be a good Dark Matter candidate.

495 Although SUSY searches in a R -parity violating (RPV) scenario have been extensively
 496 investigated by the particle-physics community, in this work only R -parity conserving
 497 (RPC) models, where the $\tilde{\chi}_1^0$ is assumed to be the LSP, were considered.

498 Phenomenological MSSM (pMSSM)

499 As mentioned in 1.2.2, once the SUSY soft breaking occurred, the unconstrained MSSM
 500 has more than 100 parameters in addition to the Standard Model ones. However, this
 501 makes the SUSY searches, e. g. finding regions, in parameter space, that are consistent
 502 with the data, rather impractical. Under the following three assumptions;

- 503 • no new source of CP-violation (CKM matrix is the only source)
- 504 • no Flavour Changing Neutral Currents
- 505 • first- and second-generation universality

506 the number of free parameters can be reduced down to 19. The introduction of such
 507 parameters, summarised in Table 1.3, defines the so-called phenomenological MSSM
 508 (pMSSM).

Table 1.3: Parameters in the pMSSM.

Parameter	Description	N. of parameters
M_1, M_2, M_3	Bino, Wino and gluino masses	3
M_A	pseudoscalar Higgs boson mass	1
μ	higgsino mass	1
$m_{\tilde{q}}, m_{\tilde{u}_R}, m_{\tilde{d}_R},$ $m_{\tilde{Q}_L}, m_{\tilde{t}}, m_{\tilde{b}}$	first- and second-generation squark masses third generation squark masses	3 3
$m_{\tilde{l}}, m_{\tilde{e}_R}$ $m_{\tilde{L}}, m_{\tilde{\tau}_R}$	first- and second-generation slepton masses third-generation slepton masses	2 2
A_t, A_b, A_τ	third-generation trilinear couplings	3
$\tan \beta$	two-higgs-doublet fields VEVs ratio	1

509 Such parameter space is still rather large and it makes pMSSM searches extremely chal-
 510 lenging and difficult to exclude. To overcome this problem *simplified models* are intro-
 511 duced. In other words, a certain signal process is extracted from the model and only
 512 particles contributing to a certain decay mode will be considered, e. g. $\tilde{t}_1 \rightarrow t + \tilde{\chi}_1^0$ only

targets the 2-body decay ignoring the remaining SUSY mass spectrum. The number of parameters will then boil down to 2; $m_{\tilde{t}}$ and $m_{\tilde{\chi}^0}$, allowing the reinterpretation of the results and providing a powerful tool to constrain various models.

In this work only analyses based on such simplified models will be presented.

Phenomenology of the top squark

Fig. 1.6 shows SUSY particles production cross-sections in pp collisions at $\sqrt{s} = 13$ TeV for squarks that do not contribute to gluino production diagrams and vice versa, i.e. treating squarks and gluinos as *decoupled* making the cross-section of squark pair-production be the same for all families. While gluino pair-production cross-sections are fairly large, SUSY electroweak production cross-sections of neutralinos and charginos are considerably lower. Slepton production cross-section, which is not displayed, would sit just below higgsino-like chargino/neutralino production cross-section.

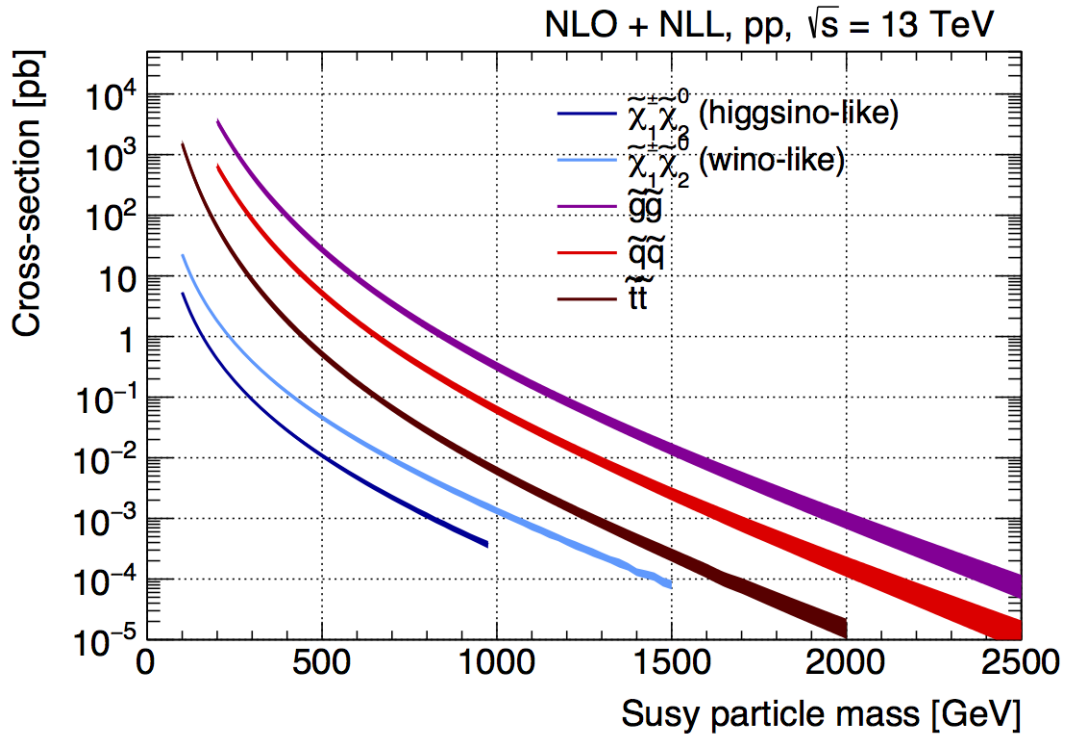


Figure 1.6: NLO+NLL production cross-sections as a function of mass at $\sqrt{s} = 13$ TeV [2]

There exists various decay modes of pair-produced stops, depending on the masses of the decay products;

- $\tilde{t} \rightarrow t \tilde{\chi}_1^0$
- $\tilde{t} \rightarrow b \tilde{\chi}_1^\pm \rightarrow b W \tilde{\chi}_1^0$ (on/off-shell W) or $\tilde{t} \rightarrow b W \tilde{\chi}_1^0$ (off-shell top)
- $\tilde{t} \rightarrow c \tilde{\chi}_1^0$
- $\tilde{t} \rightarrow b f f' \tilde{\chi}_1^0$

⁵³¹ Figure 1.7 shows a schematic representation of the parameter space $(m_{\tilde{t}_1}, m_{\tilde{\chi}_1^0})$ and
⁵³² the different region where each of the above-mentioned process dominates.

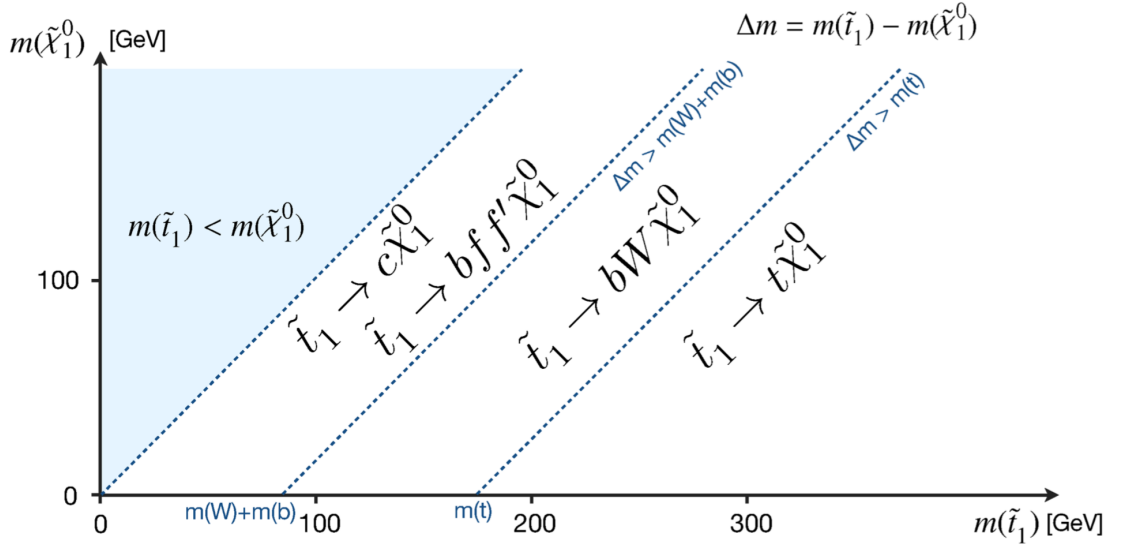


Figure 1.7: Illustration of stop decay modes in the $(m_{\tilde{t}_1}, m_{\tilde{\chi}_1^0})$ mass place where the $\tilde{\chi}_1^0$ is assumed to be the lightest supersymmetric particle. The dashed blue lines indicate thresholds separating regions where different processes dominate.

⁵³³ In the models considered in this work, either $\tilde{\chi}_2^0$ or $\tilde{\chi}_1^\pm$ is assumed to be the so-called
⁵³⁴ next lightest supersymmetric particle (NLSP). Three different decay scenarios were con-
⁵³⁵ sidered in this work; (a) where both top squarks decay via $\tilde{t} \rightarrow t^{(*)} \tilde{\chi}_1^0$; (b) at least one
⁵³⁶ of the stops decays via $\tilde{t} \rightarrow b \tilde{\chi}_1^\pm \rightarrow b W^{(*)} \tilde{\chi}_1^0$; (c) where $m_{\tilde{\chi}_2^0}$ is small enough to allow
⁵³⁷ one stop to decay via $\tilde{t} \rightarrow t \tilde{\chi}_2^0 \rightarrow h/Z \tilde{\chi}_1^0$. Here, h is the SM Higgs boson (125 GeV),
⁵³⁸ as illustrated in Figure 1.8(a)–(c), respectively. Furthermore, top squarks can also be in-
⁵³⁹ directly produced through the so-called gluino-mediated stop production, as shown in
⁵⁴⁰ Figure 1.8(d).

⁵⁴¹ Third-generation SUSY analyses, e. g. stop pair-production ($t\bar{t}$) or sbottom pair-production
⁵⁴² ($b\bar{b}$) are very challenging, due to the cross-section being around a factor of six smaller
⁵⁴³ than $t\bar{t}$ production (when $m_{\tilde{t}_1} \sim m_t$), which usually is one of the main backgrounds. Fur-
⁵⁴⁴ thermore, the cross-section of such processes dramatically decreases with increasing $m_{\tilde{q}}$.
⁵⁴⁵ Nonetheless, for example, searches for direct \tilde{t}_1 production with $\tilde{t}_1 \rightarrow t + \tilde{\chi}_1^0$ are sensitive
⁵⁴⁶ in a scenario where $m_{\tilde{t}_1} \gg m_t + m_{\tilde{\chi}_1^0}$ as the large E_T^{miss} , from the neutralinos, provides
⁵⁴⁷ discriminating power for $t\bar{t}$ rejection.

¹ The symbol (*) indicates the off-shell production

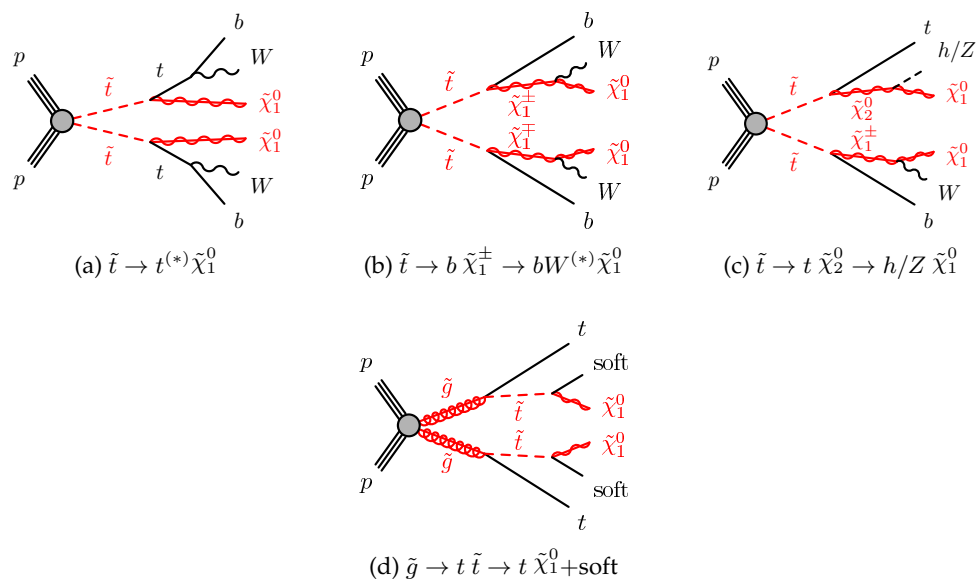


Figure 1.8: Diagrams of the decay topologies of the signal models considered in this work. The term “soft” refers to decay products that have transverse momenta below the detector thresholds.

548 | The ATLAS Experiment at the 549 LHC

550

We are rather like children, who must take a watch to pieces to see how it works.

Sir Ernest Rutherford

ATLAS (A Toroidal LHC ApparatuS) is one of the four main experiments (ATLAS, CMS, ALICE, LHCb) taking data at a center-of-mass energy of 13 TeV using beams delivered by the Large Hadron Collider (LHC). In this chapter an overview of the LHC will be given in Section 2.1, then the ATLAS detector will be described in Section 2.2, and finally the Trigger system, used to cleverly store the data, will be described in Section 2.3. A more in-depth description of the Trigger algorithms I have been involved in will be given in Chapter 3.

558 2.1 The LHC

559 As of today, the LHC is the world's largest and most powerful particle accelerator. It
560 was designed to help answer some of the fundamental open questions in particle phys-
561 ics by colliding protons at an unprecedented energy and luminosity. It is located at the
562 European Organisation for Nuclear Research (CERN), in the Geneva area, at a depth ran-
563 ging from 50 to 175 metres underground. It consists of a 27-kilometre ring made of su-
564 perconducting magnets, and inside it two high-energy particle beams travel in opposite
565 directions and in separate beam pipes.

The beams are guided around the ring by a strong magnetic field generated by coils - made of special electric cables - that can operate in a superconducting regime. 1232 superconducting dipole and 392 quadrupole magnets, with an average magnetic field of 8.3 T, are employed and kept at a temperature below 1.7 K, in order to preserve their superconducting properties. The formers are used to bend the beams and the latters to keep them focused while they get accelerated.

572 The collider first went live on September 2008 even though, due to a magnet quench

573 incident that damaged over 50 superconducting magnets, it has been operational since
 574 November 2009 when low-energy beams circulated in the tunnel for the first time since
 575 the incident. This also marked the start of the main research programme and the begin-
 576 ning of the so-called Run 1: first operational run (2009 - 2013).

577 Performance of the LHC

578 In June 2015 the LHC restarted delivering physics data, after a two-year break, the so-
 579 called Long Shutdown 1 (LS1), during which the magnets were upgraded to handle the
 580 current required to circulate 7-TeV beams. It was the beginning of the so-called Run 2 -
 581 second operational run (2015-2018) - during which LHC has collided up to 10^{11} bunches
 582 of protons every 25 ns at the design luminosity¹ of $2 \cdot 10^{34} \text{ cm}^{-2} \text{s}^{-1}$. The definiton of the
 583 luminosity is:

$$\mathcal{L} = f \frac{n_b N_1 N_2}{4\pi\sigma_x\sigma_y} \quad (2.1)$$

584 where N_1 and N_2 are the number of protons per bunch in each of the colliding beams, f
 585 is the revolution frequency of the bunch collisions, n_b the number of proton per bunch,
 586 and σ_x and σ_y are the horizontal and vertical dimensions of the beam. The luminosity is
 587 strictly related to the number of collisions occurring during a certain experiment via the
 588 following:

$$\mathcal{N}_{\text{event}} = \mathcal{L}\sigma_{\text{event}} \quad (2.2)$$

589 where σ_{event} is the cross section of the process under investigation. It has not only collided
 590 protons but also heavy ions, in particular lead nuclei at $\sqrt{s_{NN}} = 5.02 \text{ TeV}$, at a luminosity
 591 of $10^{27} \text{ cm}^{-2} \text{s}^{-1}$ [25].

592 Acceleration stages

593 Before reaching the maximum energy, the proton beams are accelerated by smaller ac-
 594 celerators through various stages. Figure 2.1 shows a sketch of the CERN's accelerator
 595 complex. It all begins at the linear accelerator LINAC 2. Here protons are accelerated up
 596 to 50 MeV, and then injected in the Proton Synchrotron Booster (PSB) where they reach
 597 1.4 GeV. The next stage is the Proton Synchrotron (PS), which boosts the beams up to 25
 598 GeV and then the Super Proton Synchrotron (SPS) makes them reach energies up to 450
 599 GeV. Eventually, the beams are injected in bunches with a 25 ns spacing into the LHC,
 600 where they travel in opposite directions, while they are accelerated to up to 13 TeV. Once
 601 the bunches reach the maximum energy, they are made collide at four different points,
 602 inside four experiments around the ring [26].

¹ the highest luminosity the detector was designed to cope with

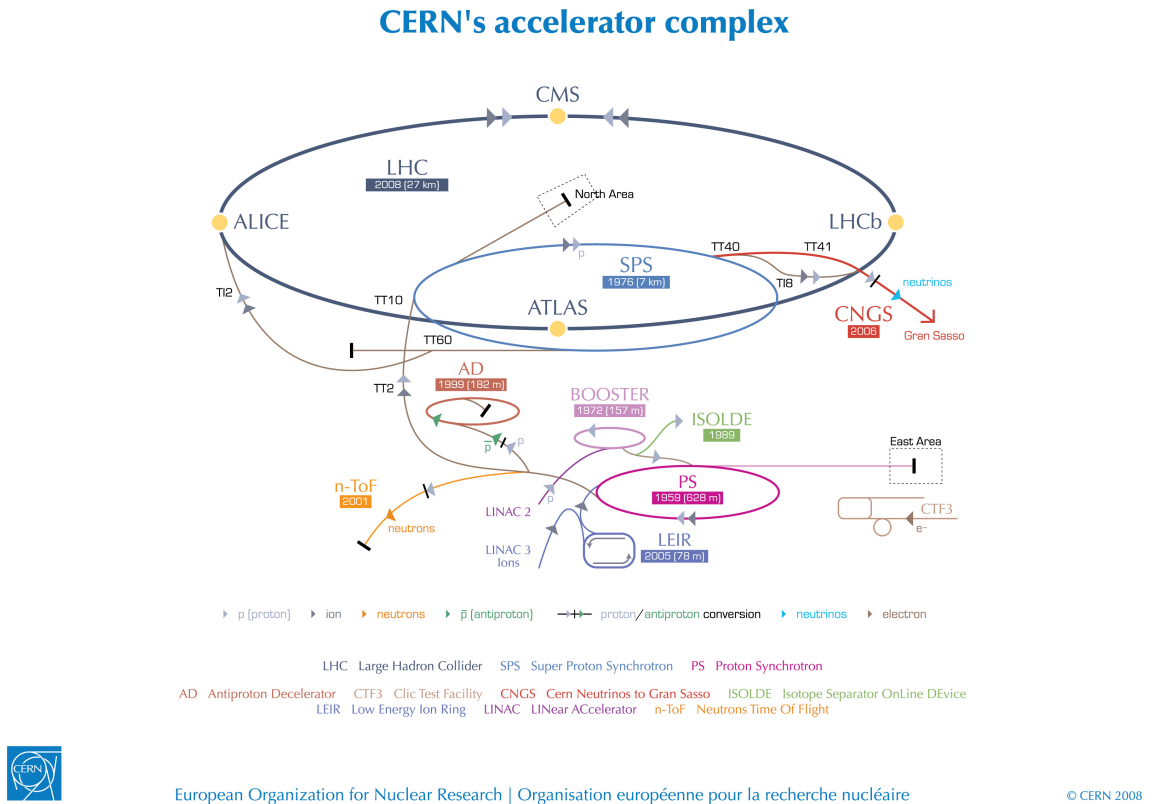


Figure 2.1: CERN Accelerator complex. The LHC is the last ring (dark grey line). Smaller machines are used for early-stage acceleration and also to provide beams for other experiments [3].

603 The heavy ion beams acceleration procedure is slightly different. Their journey starts
 604 at LINAC 3 first, and the Low Energy Ion Ring (LEIR) then, before they make their way
 605 into the PS where they follow the same path as the protons [26].

606 The four large detectors on the collision points are; the multi-purpose detectors A Tor-
 607 oidal LHC ApparatuS (ATLAS), and Compact Muon Solenoid (CMS) [27], Large Hadron
 608 Collider beauty (LHCb) [28], which focuses on flavour physics, and A Large Ion Collider
 609 Experiment (ALICE) [29] which specialises in heavy ion physics. The *big four* are not the
 610 only experiments at the CERN's accelerator complex. There also are smaller experiments
 611 based at the the four caverns about the collision points e.g. TOTEM, LHCf and MoEDAL,
 612 but this will not be discussed any further in this thesis.

613 2.2 The ATLAS Detector

614 ATLAS is a general-purpose detector designed to collect data with the highest luminosity
 615 provided by the LHC. It is located at CERN's Point 1 cavern and it measures about 45 m in
 616 length and 25 m in diameter. It has a forward-backward symmetric cylindrical geometry
 617 with respect to the interaction point and it is designed to reconstruct and measure physics
 618 objects such as electrons, muons, photons and hadronic jets. Its design was optimised to
 619 be as sensitive as possitble to the discovery of the Higgs boson and beyond-the-Standard-
 620 Model (BSM) physics. In fact, thanks to the other sub-systems, ATLAS is able to observe

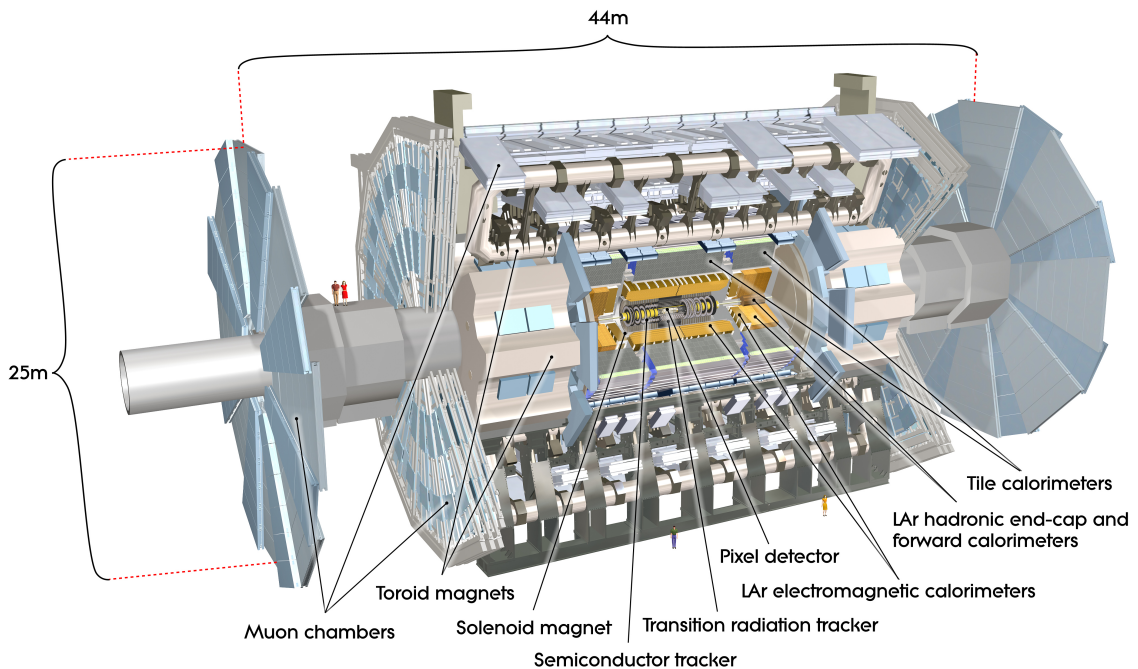


Figure 2.2: Cut-away view of the ATLAS detector. The dimensions of the detector are 25 m in height and 44 m in length. The overall weight of the detector is approximately 7000 tonnes [3].

621 all possible decay products by covering nearly 4π steradians of solid angle.

622 In Figure 2.2 a cut-away view of ATLAS with all its components is shown. The inner-
 623 most layer is the Inner Detector (ID) which is the core of the tracking system and consists
 624 of a Pixel, a Silicon micro-strip tracker (SCT), and a Transition Radiation Tracker (TRT).
 625 It is submerged in a 2 T magnetic field, generated by a thin superconducting solenoid,
 626 which bends all the charged particles' trajectories allowing transverse momentum meas-
 627 urement. The electromagnetic and hadronic calorimeters form the next layer and they are
 628 both used to perform precise energy measurements of photons, electrons, and hadronic
 629 jets. Finally, the outermost layer corresponds to the Muon Spectrometer (MS) which, to-
 630 gether with the ID, enclosed in a toroidal magnetic field, allows precise measurement of
 631 momentum and position of muons. These sub-detectors will be discussed in more detail
 632 in the following sections.

633 The ATLAS coordinate system

634 A coordinate system is taken on for the spatial definition of the sub-systems and kin-
 635 ematic measurement of physics processes. Such system is defined starting from the in-
 636 teraction point, defined as the origin. The z -axis is defined by the beam direction and the
 637 $x - y$ plan, as transverse to the beam direction.

638 A quantity, known as pseudorapidity, (η), is defined to describe the angle of a particle
 639 coming out of the collision, with respect to the beam axis:

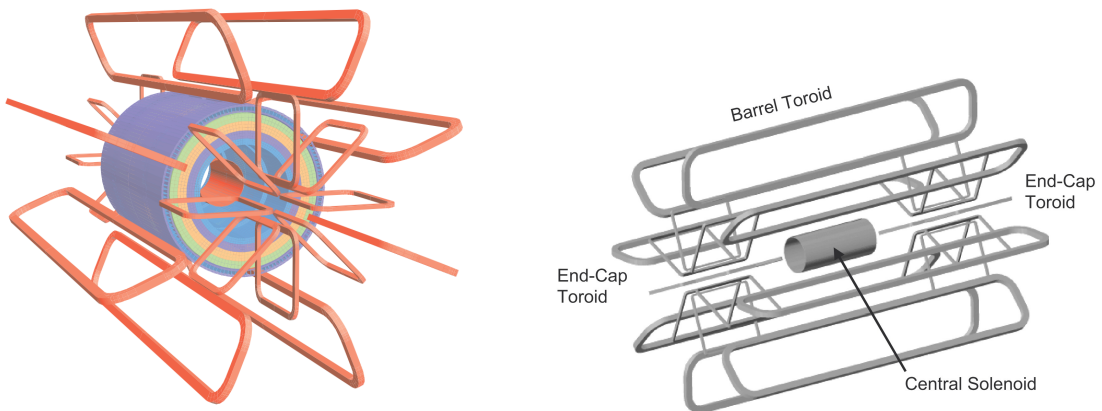
$$\eta \equiv -\ln(\tan(\theta/2))$$

640 Here θ is the polar angle. The azimuthal angle, ϕ , is defined around the beam axis and
 641 the polar angle. In the (η, ϕ) space a distance ΔR can be therefore defined as

$$\Delta R = \sqrt{\Delta\eta^2 + \Delta\phi^2}$$

642 where $\Delta\eta$ and $\Delta\phi$ are the differences in pseudorapidity and azimuthal angle between
 643 any two considered objects. A central and a forward region of pseudorapidity are also
 644 defined such that the detector components are described as part of the *barrel* if they belong
 645 to the former or as part of the *end-caps* if they belong to the latter.

646 2.2.1 The Magnet System



(a) Geometry of magnet windings and tile calorimeter steel. The eight barrel toroid coils, with the end-cap coils interleaved are visible. The solenoid winding lies inside the calorimeter volume [4].

(b) Schematic view of the superconducting magnets [30].

Figure 2.3: The ATLAS magnet system.

647 The ATLAS magnet system, 26 m long with a 22 m diameter, generates the magnetic
 648 field needed to bend the trajectories of charged particles in order to perform momentum
 649 measurement. Figure 2.3a and 2.3b show the geometry of the system and its compo-
 650 nents, which are made of NbTi - superconducting material - and will be described in the
 651 following paragraphs.

652 The Central Solenoid

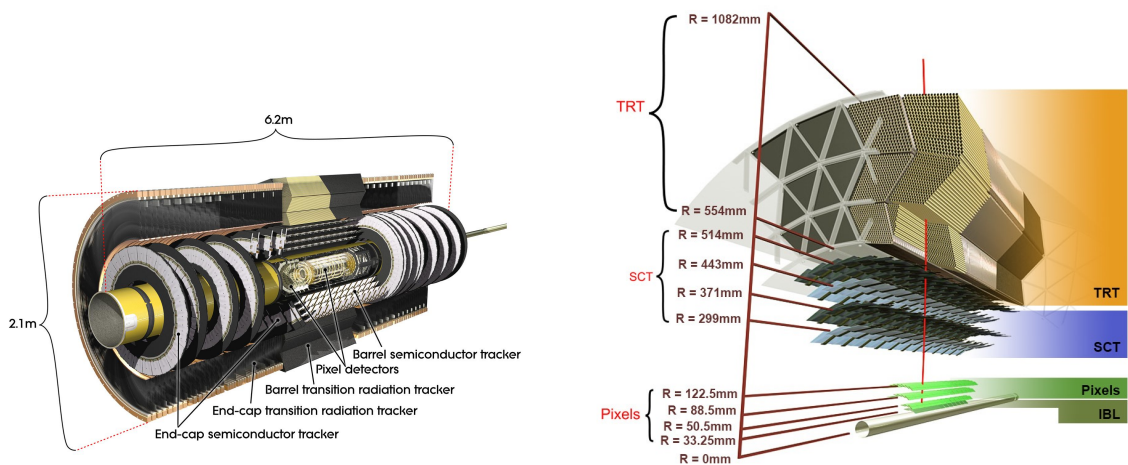
653 With an axial length of 5.8 m, an inner radius of 2.46 m, and an outer radius of 2.56 m, the
 654 central solenoid magnet is located between the ID and the ECAL. Its function is to bend
 655 the charged particles that go through the ID and it is aligned on the beam axis providing a
 656 2 T axial magnetic field that allows accurate momentum measurement up to 100 GeV [30].

657 **The Barrel and the End-cap Toroids**

658 Figure 2.3b displays the toroid magnetic system that surrounds the calorimeters. With
 659 its cylindrical shape this component consists of a barrel and two end-caps toroids, each
 660 with eight superconducting coils. The system allows accurate measurement of muon
 661 momenta using a magnetic field of approximately 0.5 T (barrel) for the central regions
 662 and 1 T (end-cap) for the end-cap regions, respectively, which bends the particles in the
 663 θ direction.

664 **2.2.2 The Inner Detector**

665 The Inner Detector (ID) [31] is the innermost component of the ATLAS detector i. e. the
 666 nearest sub-detector to the interaction region and it is used to reconstruct charged particle
 667 tracks used in the selection of physics objects. In fact, it allows robust track reconstruc-
 668 tion, with accurate impact parameter resolution ($\sim 20\mu\text{m}$) and precise primary and sec-
 669 ondary vertex reconstruction for charged particles (tracks) above 500 MeV and within
 670 $|\eta| < 2.5$.



(a) Overview of the ATLAS ID with labels and di-
mensions.

(b) Diagram of the ATLAS ID and its sub-detectors.

Figure 2.4: The ATLAS Inner Detector

671 The ID is comprised of independent and concentric sub-systems, which are all shown
 672 in Figure 2.4:

- 673 • Insertable B-Layer (IBL):
 674 innermost Pixel Detector layer added during ATLAS Run 2 upgrade (2013/2014) to
 675 improve vertexing and impact parameter reconstruction;
- 676 • Silicon Pixel Tracker (Pixel):
 677 made of silicon pixel layers and used mainly for reconstructing both the primary
 678 and secondary vertices in an event;

- 679 • SemiConductor Tracker (SCT):
 680 comprised of silicon microstrip layers; thanks to its resolution ($17 \times 580 \mu\text{m}$) it can
 681 accurately measure particle momenta;
- 682 • Transition Radiation Tracker (TRT):
 683 final layer comprised of various layers of gaseous straw tube elements surrounded
 684 by transition radiation material.

685 These sub-detectors will be discussed in the following sections.

686 IBL

687 The IBL [32] is the innermost Pixel Detector layer as shown in Figure 2.4b. It is comprised
 688 of 6M channels and each pixel measures $50 \times 250 \mu\text{m}$. Its resolution is $8 \times 40 \mu\text{m}$, The
 689 addition of this new layer brought a considerable improvement on the performance of the
 690 Pixel Detector by enhancing the quality of impact parameter reconstruction of tracks. In
 691 particular, this was achieved by improving the vertex finding efficiency and the tagging
 692 of bottom-quark-initiated jets (b -jets) which, in case of a B-layer failure, can be restored
 693 by the IBL. Besides these improvements, the IBL insertion allowed ATLAS to better cope
 694 with high luminosity effects such as the increase in event pile-up, which leads to high
 695 occupancy and read-out inefficiency.

696 Pixel

697 The Pixel detector is comprised of 1750 identical sensorchip-hybrid modules, each cover-
 698 ing an active area of $16.4 \times 60.8 \text{ mm}$. The total number of modules correspond to roughly
 699 80 million semiconductor silicon pixels. The nominal pixel size is $50 \mu\text{m}$ in the ϕ direction
 700 and $400 \mu\text{m}$ in the barrel region, along the z -axis (beam axis) [33]. The reason why such a
 701 large amount of pixels is employed is justified by the need to cope with the high luminos-
 702 ity in ATLAS. The silicon pixel detector measures 48.4 cm in diameter and 6.2 m in length
 703 providing a pseudorapidity coverage of $|\eta| < 2.5$. Figure 2.4b shows the three concentric
 704 barrel layers placed at 50.5 mm, 88.5 mm and 122.5 mm respectively. Furthermore, the
 705 Pixel detector is made of six disk layers, three for each forward region, such that when a
 706 charged particle crosses the layers it will generate a signal at least in three space points.
 707 The fine granularity of such detector allows accurate measurement and precise vertex
 708 reconstruction, as it provides a more accurate position measurement as a large detection
 709 area is available. In particular, it has a resolution of $10 \times 115 \mu\text{m}$.

710 SCT

711 The SCT is made of 4088 modules of silicon micro-strip detectors arranged in four con-
 712 centric barrel layers. It is mainly used for precise momentum reconstruction over a range
 713 $|\eta| < 2.5$ and it was designed for precision measurement of the position using four points

⁷¹⁴ (corresponding to eight silicon layers), obtained as track hits when crossing the layers.
⁷¹⁵ Figure 2.4b shows the structure of the SCT with its four concentric barrel layers with
⁷¹⁶ radii ranging from 299 mm to 514 mm and two end-cap layers. Each module has an
⁷¹⁷ intrinsic resolution of $17 \mu\text{m}$ in the $R - \phi$ direction and $580 \mu\text{m}$ in the z direction. As
⁷¹⁸ the SCT is further away from the beam-pipe than the Pixel detector, it has to cope with
⁷¹⁹ reduced particle density. This allows for reduced granularity maintaining the same level
⁷²⁰ of performance of the Pixel detector: SCT can use ~ 6.3 million read-out channels.

⁷²¹ TRT

⁷²² The last and outermost of the sub-systems in the ID is the TRT. It is a gaseous detector
⁷²³ which consists of 4 mm diameter straw tubes wound from a multilayer film reinforced
⁷²⁴ with carbon fibers and containing a $30 \mu\text{m}$ gold plated tungsten wire in the center. The
⁷²⁵ straw is filled with a gas mixture of 70% Xe, 27% CO₂ and 3% O₂ [34]. As shown in Fig-
⁷²⁶ ure 2.4b, its section consists of three concentric layers with radii ranging from 544 mm to
⁷²⁷ 1082 mm, each of which has 32 modules containing approximately 50,000 straws, 1.44 m
⁷²⁸ in length, aligned parallel to the beam direction with independent read-out at both ends.
⁷²⁹ Both end-cap sections are divided into 14 wheels, with roughly 320,000 straws in the R-
⁷³⁰ direction. The average 36 hits per track in the central region of the TRT allow continuous
⁷³¹ tracking to enhance pattern recognition and momentum resolution in the $|\eta| < 2.5$ region.
⁷³² It also improves the p_{T} resolution for longer tracks.

⁷³³ 2.2.3 The Calorimeters

⁷³⁴ The ATLAS Calorimeter system, shown in Figure 2.5, is comprised of two main sub-
⁷³⁵ systems; the electromagnetic calorimeter (ECAL) and hadronic calorimeter (HCAL), which
⁷³⁶ are designed to stop and measure the energy of electromagnetic-interacting and had-
⁷³⁷ ronic particles respectively. The combination of the two provides full coverage in ϕ and
⁷³⁸ $|\eta| < 4.95$. Particles slow down and lose energy generating showers when crossing dif-
⁷³⁹ ferent layers. The ECAL is comprised of one barrel and two end-cap sectors employing
⁷⁴⁰ liquid Argon (LAr). The showers hereby develop as electrons pairs which are then col-
⁷⁴¹ lected. The HCAL is also comprised of one barrel and two end-cap sectors. The sensors
⁷⁴² in the barrel of the HCAL are tiles of scintillating plastic whereas LAr is employed for
⁷⁴³ the end-cap. A forward region, the closest possible to the beam, is covered by a LAr for-
⁷⁴⁴ ward calorimeter (FCal). The LAr and Tile Calorimeter will be briefly discussed in the
⁷⁴⁵ following paragraphs.

⁷⁴⁶ The Liquid Argon Calorimeters

⁷⁴⁷ The ECAL is comprised of multiple layers of liquid Argon (LAr) sampler and lead ab-
⁷⁴⁸ sorber. The choice of its accordion-geometry design brought two main advantages; full
⁷⁴⁹ ϕ coverage with no non-interactive regions (no cracks); fast extraction of signals coming

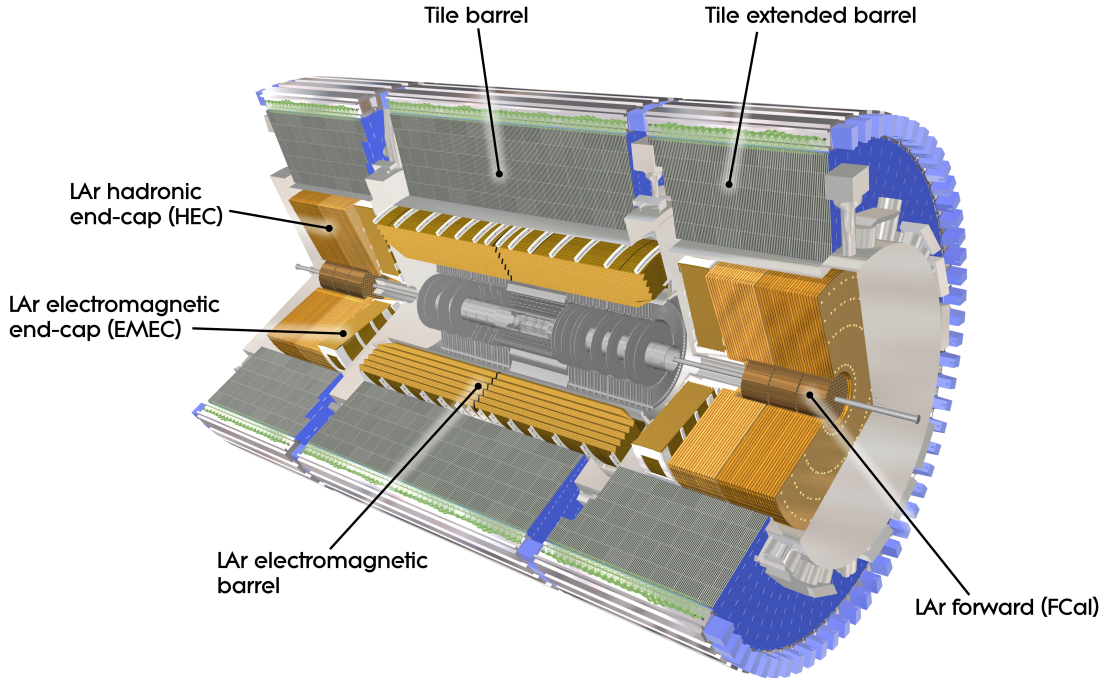


Figure 2.5: A computer generated image of the full calorimeter.

from both front or rear end of the electrodes. It is made of two half-barrel wheels, both placed in the barrel cryostat, that provide a pseudorapidity coverage up to $|\eta| < 1.475$ and two end-cap detectors providing $1.375 \leq |\eta| \leq 3.20$ coverage in two end-cap cryostats. The junction between the barrel and end cap components defines the crack region and any signal coming from the crack region is therefore discarded.

In the $|\eta| < 1.8$ region there is an additional layer, placed at the front of the calorimeter, that is made of a thin (0.5 cm in the end-cap and 1.1 cm in the barrel) LAr layer with no absorber [35]. This additional layer was designed to correct for the energy lost, as particles enter the calorimeter, by taking a measurement just before the majority of the electromagnetic shower is developed.

Two separate readout paths are employed: one with coarse granularity (*trigger towers*), and one with fine granularity. These which will be further discussed in Chapter 3.

762 The Tile calorimeter

763 The main purpose of the hadronic calorimeter is to measure the energy of hadronic
 764 showers. It is built employing steel and scintillating tiles coupled to optical fibres which
 765 are read out by photo-multipliers. As shown in Figure 2.5, the HCAL is made up of three
 766 cylinders; a central barrel, 5.64 m long covering a region $|\eta| < 1.0$, and two extended
 767 barrel, 2.91 m long covering a reigon $0.8 < |\eta| < 1.7$. Each cylinder is made up of 64
 768 modules and each module is in turn made up of three layers. Ultimately, the smallest
 769 section of the calorimeter module is a cell with a $\Delta\phi \times \Delta\eta = 0.1 \times 0.1$ granularity for the

⁷⁷⁰ two innermost layers and $\Delta\phi \times \Delta\eta = 0.2 \times 0.1$ for the outermost one.

⁷⁷¹ 2.2.4 The Muon Spectrometer

⁷⁷² The MS [36], shown in Figure 2.6, is the outermost sub-system of the whole ATLAS de-
⁷⁷³ tector. As such, it surrounds the calorimeters and its main function is to perform precision
⁷⁷⁴ measurement of muons momenta. The deflection of muon tracks employing large super-
⁷⁷⁵ conducting air-core toroid magnets and high-precision tracking chambers is at the heart
⁷⁷⁶ of such high precision measurement.

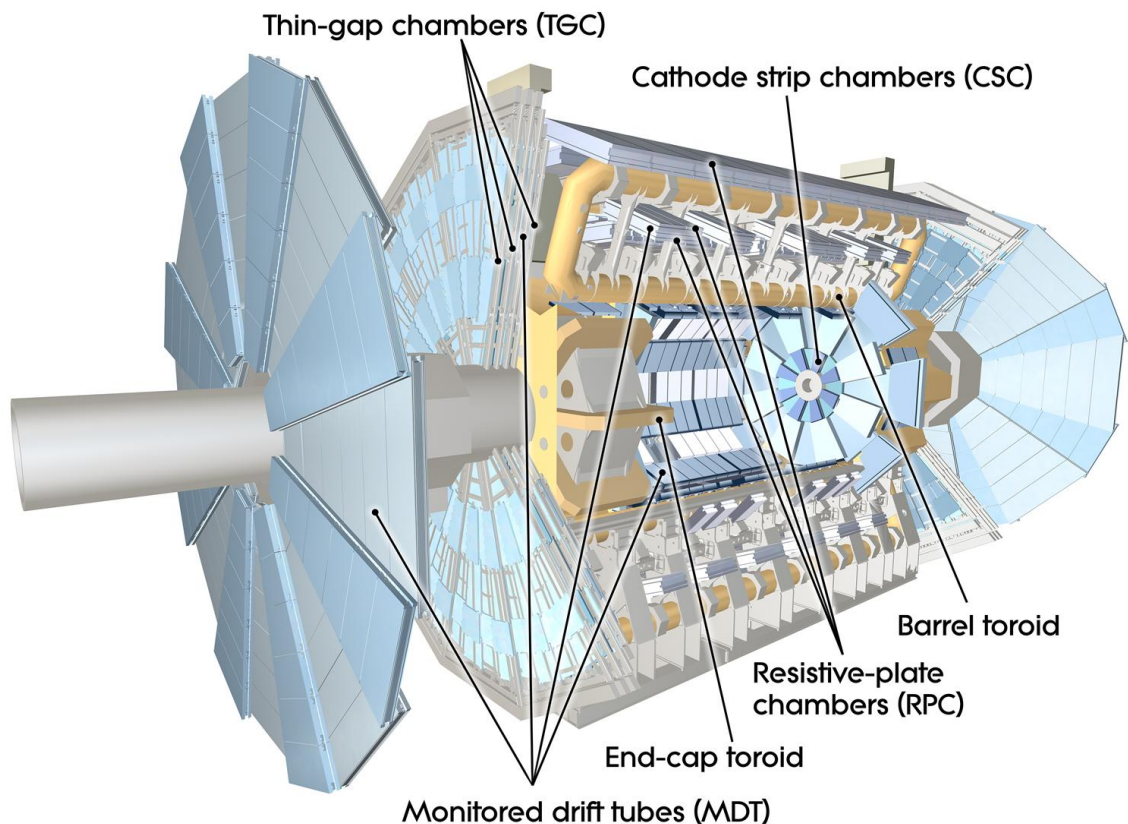


Figure 2.6: Cut-away view of the ATLAS muon system [4].

⁷⁷⁷ The MS is comprised of one large barrel toroid, covering the region $|\eta| \leq 1.4$, and two
⁷⁷⁸ end-cap toroids, covering $1.6 < |\eta| \leq 2.7$ which are employed together to achieve the
⁷⁷⁹ track-bending effect wanted. The magnitude of the magnetic field in the barrel, generated
⁷⁸⁰ by eight large superconducting coils, ranges from 0.5 to 2 T.

⁷⁸¹ Around the beam axis, three cylindrical layers make way for the chambers, placed in
⁷⁸² planes perpendicular to the beam, used to measure tracks.

⁷⁸³ Monitored Drift Chambers (MDTs) are employed over most of the pseudorapidity
⁷⁸⁴ range to provide precision measurement of track coordinates in the bending direction.
⁷⁸⁵ An MDT is essentially a set of 30-mm-diameter Al tubes containing a W-Re wire, surroun-
⁷⁸⁶ ded by a non-flammable Ar – CH₄ – N₂ mixture at a pressure of 3 bar. The resolution a
⁷⁸⁷ single wire can give on the particle position is 80 μm enhanced by having multiple layers

788 of tubes for each module.

789 Cathode Strip Chambers (CSCs) are instead employed at large pseudorapidity ($2 <$
790 $|\eta| < 2.7$). They work similarly to the MDT but instead of tubes there are cathode strips
791 above and below the anode wires. In particular, one set is orthogonal to the wires for
792 precision measurement and the other one parallel to the wires providing a measurement
793 of the transverse coordinate. The gas employed between the strips and wires is a non-
794 flammable mixture of Ar – CO₂ – CF₄.

795 Finally, Thin-Gap Chambers (TGCs) are employed in the end-cap region and Resistive-
796 Plate Chambers (RPCs) in the barrel. The TGCs are very similar to the CSCs. They
797 provide large signals and in a very narrow time window making them ideal for trig-
798 gering purposes.

799 The RPC is also a gas-based detector. It is comprised of two parallel resistive plates
800 held apart by insulating spacers, and a uniform electric field is employed to generate a
801 limited avalanche multiplication centred around the primary ionisation electron. This
802 will then be detected by Al strips separated from the plates by an insulating film.

803 TGCs and RPC will be mentioned again in [3.2](#) as they are part of the trigger system.

804 2.3 The ATLAS Trigger System

805 The ATLAS Trigger System is at the heart of data taking. It is an essential component of
806 any nuclear or particle physics experiment as it is responsible for deciding whether or
807 not to store an event for later study. Its main function to reduce the event rate from ~ 40
808 MHz bunch-crossing² to ~ 1 kHz.

809 The Trigger system employs a two-level system: a first hardware-based level trig-
810 ger, *Level 1 Trigger* (L1), and a software-based *high-level trigger* (HLT). L1 processes low-
811 granularity information from the calorimeter and the muon spectrometer and identifies
812 the so-called Regions of Interest (RoIs)³ before making a decision. Event data from other
813 sub-systems are temporarily stored in memories whilst L1 decision is taken.

814 Further investigations are left to HLT which is made of software running on a cluster
815 of computers (HLT farm). Additionally, a Fast TracKer (FTK) system [37] (to be installed
816 before the end of Run 2) will process events that are accepted by L1 trigger, and seed the
817 HLT algorithms. It will provide global ID track reconstruction at the L1 trigger rate using
818 lookup tables stored in custom associative memory chips for the pattern recognition.

819 The ATLAS trigger system will be further discussed in Chapter [3](#), however the Run-
820 1-to-Run-2 upgrade of the ATLAS trigger will not be discussed any further.

² The term bunch-crossing, $\langle \mu \rangle$, is hereby used when referring to a collision between two bunches of protons.

³ $\eta - \phi$ regions where event features have been found by the L1 selection process.

821 3 | The ATLAS Trigger System

822

*In God we trust. All others must
bring data.*

W. Edwards Deming

823 The ATLAS trigger system together with its performance will be presented in this
 824 chapter. A brief introduction, about the reason behind the need of a trigger system to-
 825 gether with its implementation in ATLAS will be discussed in Section 3.1. The Level-1
 826 and High-Level triggers will be discussed in Sections 3.2 and 3.3, respectively. Finally,
 827 Section 3.3.2 will be dedicated to the performance of HLT for low- p_T single-lepton, and
 828 medium- and high- p_T b -jet triggers - as part of the *qualification task*¹ of the author -, to-
 829 gether with the missing transverse energy, E_T^{miss} , trigger performance - as the most relev-
 830 ant trigger for the analysis discussed in Chapter 5.

831 3.1 Overview

832 More than 80 fb^{-1} of pp collisions were delivered in 2016 and 2017 by the LHC and due
 833 to storage space limitations it is not feasible to save all the information about the collision
 834 after every bunch crossing, so the ATLAS Trigger System is indispensable to reduce the
 835 read-out rate to a sensible value without affecting the physics programme of ATLAS,
 836 e. g. discarding potentially interesting events. A multiple-level architecture is employed
 837 to allow the trigger some more time such that the identification, of an interesting event,
 838 using both software- and hardware-based real-time algorithms to determine whether or
 839 not a bunch-crossing contains interesting physics, is made possible.

840 Figure 3.1 shows the Trigger and Data Acquisition (TDAQ) system. This is comprised
 841 of both a hardware-based first-level trigger (L1) and a software-based high-level trigger
 842 (HLT), as already anticipated in Section 2.3. The L1 trigger decision is formed by the Cen-
 843 tral Trigger Processor (CTP), which receives inputs from the L1 calorimeter (L1Calo) and
 844 L1 muon (L1Muon) triggers. Once the events passed L1 selection, they are buffered in
 845 the Read-Out System (ROS) and processed by the HLT, which receives Region-of-Interest

¹ In order to become an ATLAS author, a person must have been an active ATLAS member for at least one year working on a technical work

- 846 (RoI) information from L1 to be used for track reconstruction in the trigger algorithms.
 847 Events accepted by HLT are then transferred to local storage and exported to the *Tier-0*
 848 facility at CERN's computing centre for offline reconstruction.

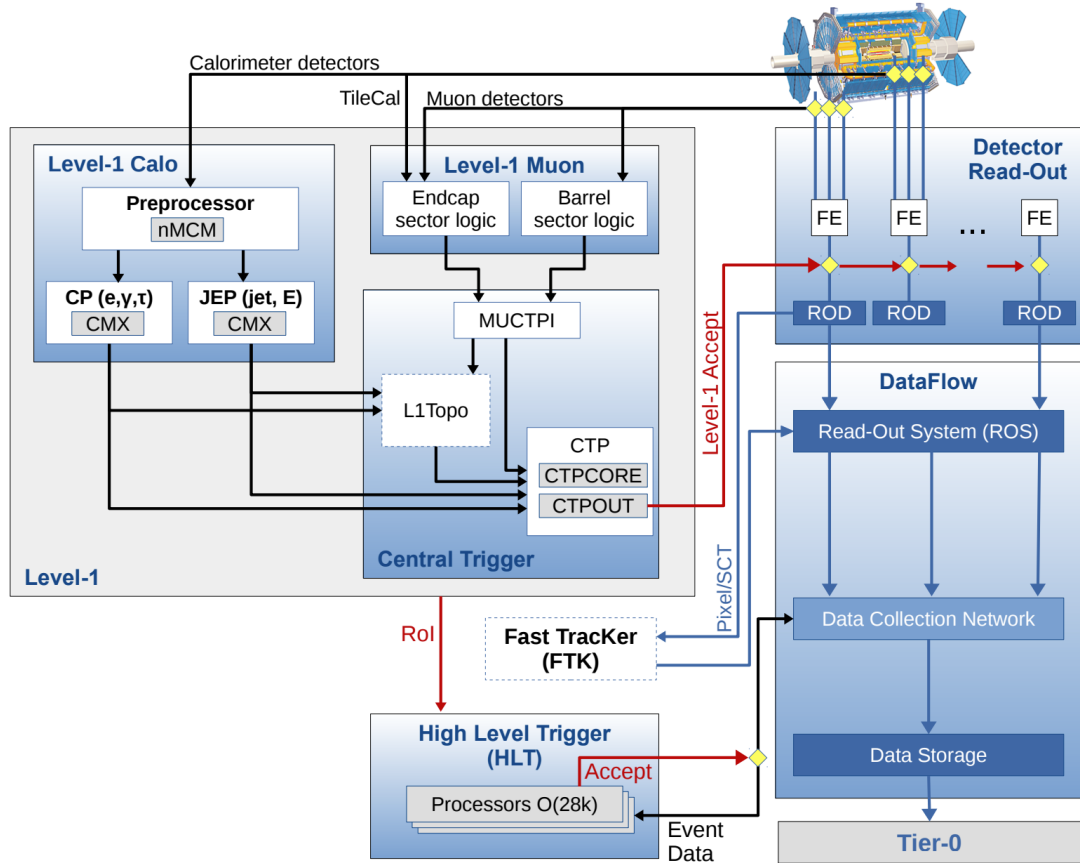


Figure 3.1: The ATLAS TDAQ system. L1Topo and FTK [5] have not been used for the results shown in this thesis.

849 The trigger system is configured via the so-called trigger *menu* that is meant to define
 850 the trigger *chains* - usually referred to just as trigger - that start from a L1 trigger and
 851 specify a sequence of reconstruction and selection steps for the specific trigger signatures
 852 required in the trigger chain. Figure 3.2 shows an illustration of an electron-trigger chain
 853 used to select electrons [6].

854 3.2 Level-1 Trigger

855 The L1 trigger decision is essentially taken by the Central Trigger Processor (CTP), based
 856 on the information the L1 calorimeter and L1 muon trigger systems. Additionally, a to-
 857 pological trigger (L1Topo)², fed with energy and direction information about the objects
 858 found by the L1 calorimeter and L1 muon triggers, is employed [4, 5, 38].

² Two FPGA-based (Field-Programmable Gate Arrays) processor modules

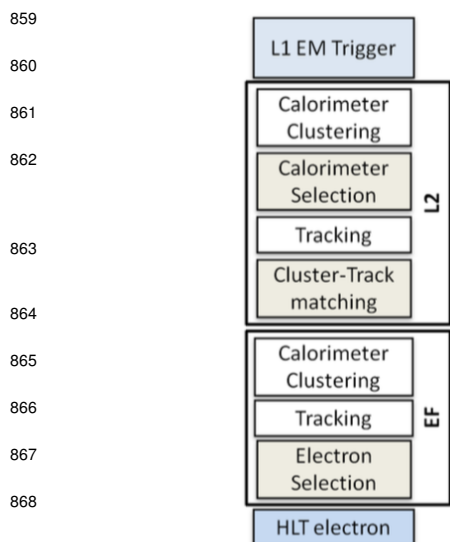


Figure 3.2: An Electron-trigger chain (from [6]).

The L1 trigger system is implemented in fast custom electronics to keep the decision time around $2.5 \mu\text{s}$ and its decision is used as a *seed* for HLT.

3.2.1 The CTP

The CTP [4] applies the multiplicity requirements and prescale factors specified in the trigger menu to the inputs from the L1 trigger systems and forms the L1 trigger decision. Timing and control signals³ are employed to distribute the L1 trigger decision to all ATLAS sub-detector readout systems. It is responsible for applying the so-called *preventive dead-time*, meant to limit the minimum time between

two consecutive L1 accepts (*simple dead-time*), $\mathcal{O}(100\text{ns})$, in order to both avoid overlapping readout windows, and restrict the number of L1 accepts allowed in a given number of bunch-crossings (*complex dead-time*) to avoid buffers from overflowing. In addition, a *busy dead-time*, can be introduced by ATLAS sub-detectors to temporarily throttle the trigger rate. These dead-times are used to monitor the total L1 trigger rate, and individual trigger rates that need to be monitored before and after any prescales and/or any vetoes that have been applied. Furthermore, such information is also used to provide a measure of the L1 dead-time, which has to be accounted for when determining the luminosity [6].

3.2.2 The L1 Calorimeter Trigger

The L1 calorimeter trigger [4, 39] is based on inputs from the electromagnetic and hadronic calorimeters within the region $|\eta| < 4.9$. It provides triggers for objects such as electrons/photons, taus, jets, and global transverse energy. Dedicated analogue trigger signals, provided by the ATLAS calorimeters independently from the signals read out and used at the HLT and offline, make the L1 calorimeter trigger decision, which is based on the information from analogue sums of calorimeter elements, called *trigger towers*, instead of using the full granularity of the calorimeter. The trigger towers have a size of approximately $\Delta\eta \times \Delta\phi = 0.1$ in the central part of the calorimeter, $|\eta| < 2.5$, and they get larger and less regular in the forward region. Separate trigger towers are employed for electromagnetic and hadronic calorimeters. Furthermore, two processor systems run the trigger algorithms, once the signals have been digitised: the first, called *cluster processor*,

³ The timing signals are defined with respect to the LHC bunch crossings: a 25 ns time window centred on the instant at which a proton bunch might cross the ATLAS interaction point.

uses the full L1 trigger granularity information in the central region to look for small and localised clusters, which are typical energy deposit left by an electron, photon or tau; the second, the *jet and energy-sum processor*, uses 2×2 sums of trigger towers (jet elements), to identify jet candidates and form missing transverse energy, E_T^{miss} , and total transverse energy, E_T . As an example, Figure 3.3 shows a sketch of the electron/photon and tau triggers. The trigger algorithm identifies a Region of Interest as a 2×2 trigger tower cluster in the electromagnetic calorimeter for which the transverse-energy sum, released in at least one of the four possible pairs of nearest neighbour towers (1×2 or 2×1), exceeds a pre-defined threshold. Additionally, jets RoIs are defined as 4×4 , 6×6 or 8×8 trigger-tower windows for which the summed electromagnetic and hadronic transverse energy exceeds pre-defined thresholds and which surround a 2×2 trigger tower core that is a local maximum that will be also used to define the coordinates of the jet ROI.

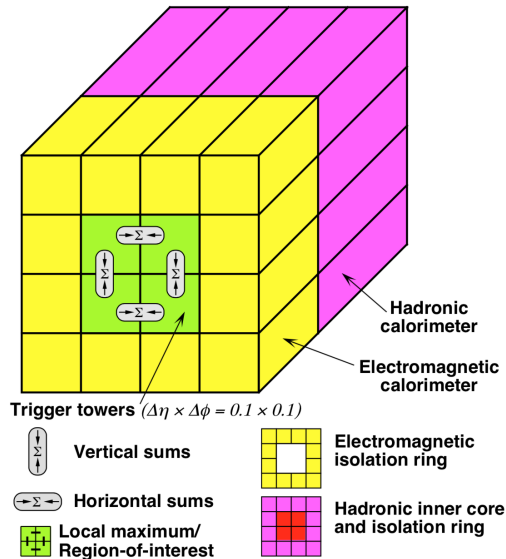


Figure 3.3: Illustration of the electron/photon and tau algorithms with the sums to be compared to programmable thresholds (from [6]).

3.2.3 The L1 Muon Trigger

The L1 Muon trigger system [40] processes input data from fast muon trigger sub-detectors and its main task is to select muon candidates with a p_T threshold of 6 GeV and identify the bunch crossing in which they were produced.

Figure 3.4 shows how muons are triggered at L1. The RPC system in the barrel region ($|\eta| < 1.05$) and the TGC system in the end-cap regions ($1.05 < |\eta| < 2.4$) are employed. They provide a rough measurements of muon-candidate p_T , η , and ϕ . Three planes in the barrel and three in each endcap form the trigger chambers. Each plane is comprised of two to four layers and muon candidates are identified by forming coincidences between the muon planes. Coincidences are formed requiring hits that lie within parametrised geometrical muon *roads*. A road, as the example shown in Figure 3.4, essentially con-

tains the trajectories, from the interaction point, of either positively or negatively charged muons with a p_T above a given threshold. In particular six programmable p_T thresholds are employed at L1, divided into two sets: three low- p_T thresholds meant to cover values up to 10 GeV, and three high- p_T thresholds meant to cover $p_T > 10$ GeV.

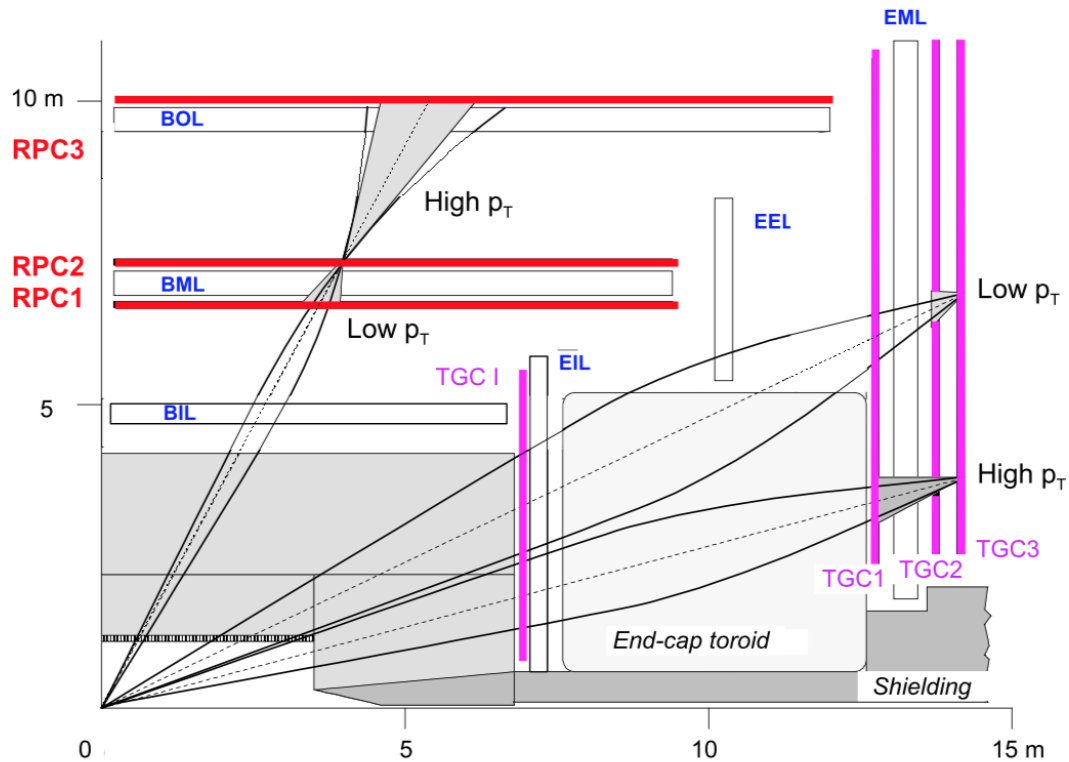


Figure 3.4: A schematic view of the L1 muon trigger chambers (from [6]).

3.3 High-Level Trigger

The events that are accepted by L1 are then buffered in the Read-Out System (ROS) and processed by the *High-Level Trigger* using information that is not available at L1, such as finer-granularity calorimeter inputs, precision measurements from the MS and tracking information from the ID. HLT receives Regions-of-Interest from L1 and performs the reconstruction within them. As needed, the reconstruction performed by the HLT software can either be run within RoIs or performing a so-called *full scan* of the detector. In order to reduce the processing time, a two-stage approach is employed for most HLT triggers: a first reconstruction (fast) to reject the majority of events; a second precision reconstruction for the remaining events (slower). Events that are accepted by the HLT get transferred to local storage at the experimental site and exported to the CERN's computing centre for offline reconstruction [5].

933 **3.3.1 Inner detector tracking**

934 The track reconstruction in the Inner Detector is a vital component of the trigger decision
935 in the HLT. A robust reconstruction of particle trajectories is an essential prerequisite for
936 triggering on electrons, muons, B-physics, taus, and b -jets. Furthermore, it is also used for
937 triggering on inclusive pp interactions and for the online determination of the beamspot⁴
938 where the reconstructed tracks provide the input for vertex reconstruction.

939 The ID tracking in the trigger also includes information from the IBL, which signifi-
940 cantly improves the tracking performance and in particular the impact parameter res-
941 olution [32]. The tracking algorithms are called *Fast Tracking* and *Precision Tracking*. The
942 former is comprised of trigger-specific pattern recognition algorithms, unlike the latter
943 which is heavily based on offline-tracking algorithms. As already mentioned, once an ROI
944 has been identified by L1, the algorithms are typically configured to run within it. Fur-
945 thermore, in order to reduce CPU usage, the offline track-finding is seeded with tracks
946 and space-points identified by fast tracking stage seeds. Running the full HLT recon-
947 struction for each event on an individual node, affords the opportunity to better optimise
948 the ROI geometry and use an advanced multi-stage strategy for the tau and b -jet triggers,
949 which will be discussed in Section 3.3.2.

950 In order to reduce the detector volume of ROI, an advanced multi-stage approach, in
951 particular for tau and b -jet tracking, is employed. The first stage is to identify leading
952 tracks within a long-in- z but narrow-in- η and ϕ ROI running the Fast Track Finder (FTF)
953 algorithm. The leading tracks are used to construct a second-stage ROI, constrained in
954 both η and ϕ , but very tightly constrained in polar angle and with a small z position
955 width. The FTF is then run again within the wider second-stage ROI, followed by the
956 Precision Tracking [41]. The second stage, the precision tracking, is heavily based on an
957 optimised subset of the tracking algorithms used offline, which is slower than the first
958 but, in return, it identifies objects constructed starting from the inner detector tracks.

959 As the future inclusion of the FTK tracks had to be taken into account, tracks provided
960 by the FTK were integrated into the system although they were not used for any of the
961 results presented in this work.

962 **3.3.2 Performance of HLT**

963 The performance of the tracking was estimated using 13-TeV pp collision collected in
964 July 2015 by the ATLAS detector, unless otherwise stated. In order to be as unbiased
965 as possible, specific monitoring triggers, that do not require a track to be present for the
966 event to be accepted, are used to estimate the efficiency of the tracking algorithms. All the
967 quantities used to estimate the performance of the tracking, i. e. efficiencies, residuals and
968 resolutions, are calculated with respect to the tracks found by the offline reconstruction

⁴ The luminous region produced by the collisions of proton beams.

software. In particular, the efficiency is defined as the fraction of offline reference tracks that are matched to a trigger track

$$\mathcal{E} = \frac{N_{\text{trigger}}}{N_{\text{offline}}} \quad (3.1)$$

The tracking efficiency has been estimated for electrons and muons for the single-stage tracking, and for b -jets for the multi-stage approach, as part of the author's qualification task. The reconstructed tracks are required to have at least two (six) pixel (SCT) clusters and lie in the region $|\eta| < 2.5$. The closest trigger track within a cone of size $\Delta R = \Delta\eta^2 + \Delta\phi^2 = 0.05$ of the offline reconstructed track is selected as the matching trigger track.

Electrons

Figure 3.5 shows the tracking efficiency for the 24 GeV electron trigger as a function of η and p_T of the offline track. The tracking efficiency is measured with respect to offline tracks with $p_T > 20$ GeV for tight offline electron candidates from the 24 GeV electron support trigger, which does not use the trigger tracks in the selection, despite being identical to the physics trigger. The FTF and Precision Tracking efficiencies are all above 99% within the whole pseudorapidity range. The small efficiency drop at low p_T is due to bremsstrahlung energy loss by electrons [5].

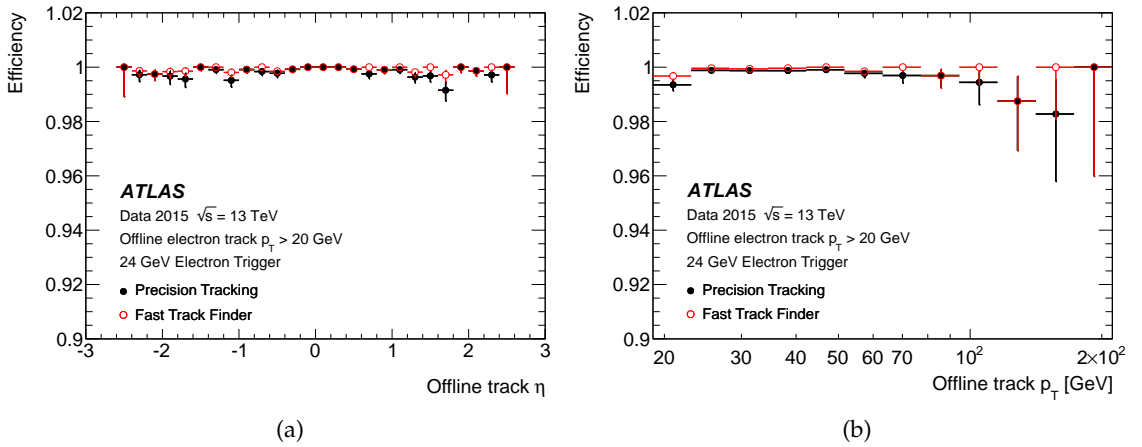


Figure 3.5: The ID tracking efficiency for the 24 GeV electron trigger is shown as a function of the (a) η and (b) p_T of the track of the offline electron candidate. Uncertainties based on Bayesian statistics are shown (from [5]).

Muons

Figure 3.6a shows the muon tracking performance with respect to offline muon candidates with $p_T > 6$ GeV selected by the 6 GeV muon support trigger as a function of the offline muon p_T . The efficiency is well above 99% in the entire p_T range for both FTF

and precision tracking. Figure 3.6b shows the resolution of the transverse track impact parameter with respect to offline as a function of the offline muon p_T . FTF and Precision Tracking resolutions are better than 17 and 15 μm , respectively, for muon candidates with offline $p_T > 20 \text{ GeV}$.

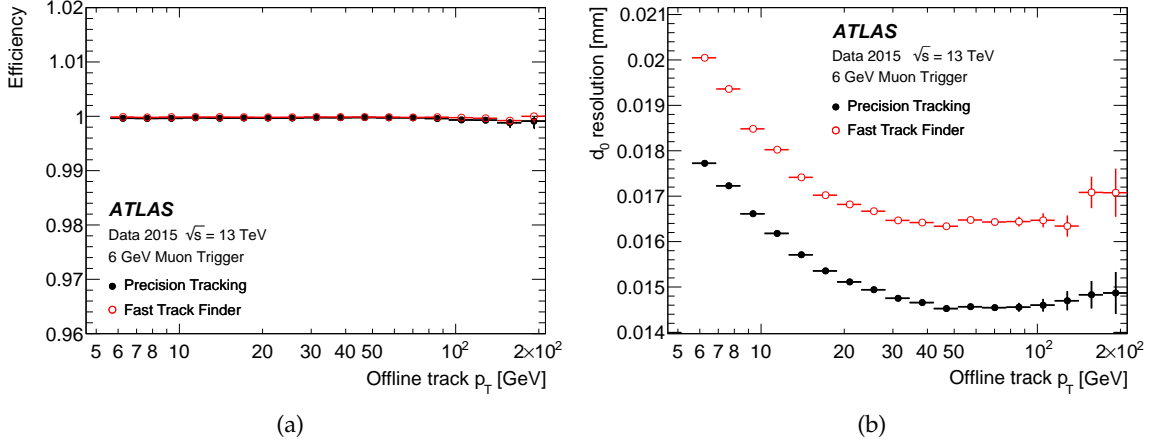


Figure 3.6: The ID tracking performance for the 6 GeV muon trigger; (a) efficiency as a function of the offline reconstructed muon p_T , (b) the resolution of the transverse impact parameter, d_0 as a function of the offline reconstructed muon p_T . Uncertainties based on Bayesian statistics are shown (from [5]).

993 ***b*-jets**

As previously mentioned, the hadronic tau and *b*-jet triggers tracking algorithms are run in a larger RoI than for electrons or muons and in order to limit CPU usage, multiple stage track reconstruction was implemented and deployed during Run-2. However, tau tracking will not be further discussed.

First, the leading track and its position along the beamline are determined by executing fast tracking in an ROI that is fully extended along the beamline, in the $|z| < 225$ mm region, but narrow (0.1) in both η and ϕ , as shown in the blue-shaded region in Figure 3.7. The second stage is then run, using this position along the beamline, to reconstruct all tracks in an ROI that is larger (0.4) in both η and ϕ but limited to $|\Delta z| < 10$ mm with respect to the leading track, as shown by the green-shaded region in Figure 3.7.

The first-stage vertex tracking takes all jets identified by the jet trigger with $\eta > 30$ GeV and reconstructs tracks with the FTF in a narrow region in η and ϕ around the jet axis for each jet, but with $|z| < 225$ mm along the beam line.

Following this step, the primary vertex reconstruction [42] is performed using the tracks from the fast tracking stage. This vertex is used to define wider ROIs around the jet axes, with $|\Delta\eta| < 0.4$ and $|\Delta\phi| < 0.4$ but with $|\Delta z| < 20$ mm relative to the primary vertex z position. These ROIs are then used for the second-stage reconstruction that runs the fast track finder in the wider η and ϕ regions followed by the precision tracking,

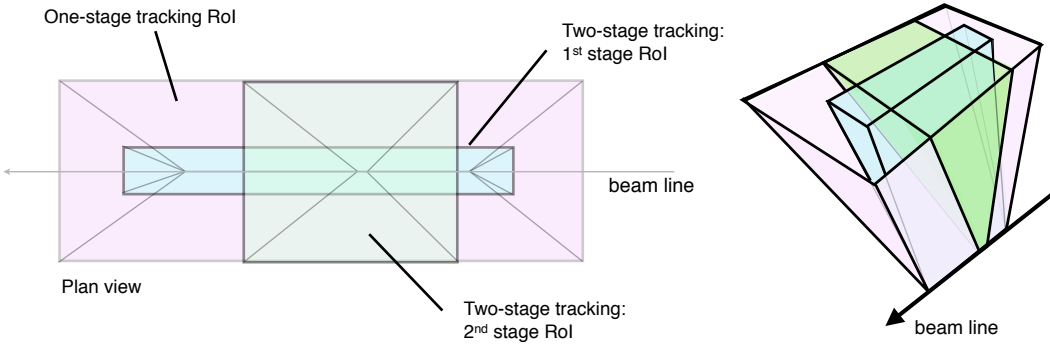


Figure 3.7: An illustration of the RoIs from the single-stage and two-stage tau lepton trigger tracking, shown in plan view (x-z plane) along the transverse direction and in perspective view. The z-axis is along the beam line. The combined tracking volume of the 1st and 2nd stage ROI in the two-stage tracking approach is significantly smaller than the ROI in the one-stage tracking scheme (from [5]).

secondary vertexing and b -tagging algorithms, which will not be discussed in this work.

The performance of the primary vertexing in the b -jet vertex tracking can be seen in Figure 3.8a, which shows the vertex finding efficiency with respect to offline vertices in jet events with at least one jet with transverse energy above 55, 110, or 260 GeV and with no additional b -tagging requirement. The efficiency is shown as a function of the number of offline tracks with $p_T > 1$ GeV that lie within the boundary of the wider ROI (defined above) from the selected jets. The efficiency rises sharply and is above 90% for vertices with three or more tracks, and rises to more than 99.5% for vertices with five or more tracks. The resolution in z with respect to the offline z position as shown in Figure 3.8b is better than 100 μm for vertices with two or more offline tracks and improves to 60 μm for vertices with ten or more offline tracks.

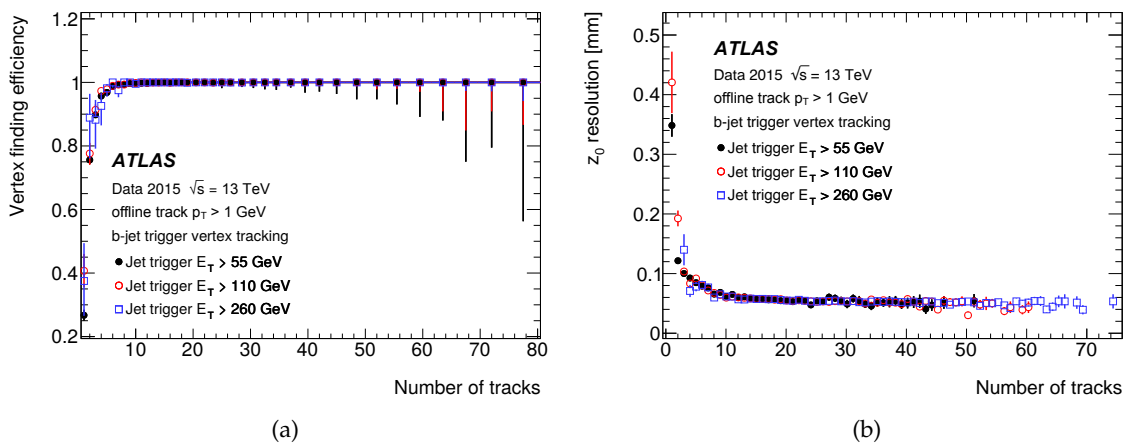


Figure 3.8: The trigger performance for primary vertices in the b -jet signatures for 55, 110 and 260 GeV jet triggers; (a) the vertexing efficiency as a function of the number of offline tracks within the jets used for the vertex tracking, (b) the resolution in z of the vertex with respect to the offline vertex position as a function of the number of offline tracks from the offline vertex (from [5]).

1023 **Missing Transverse Energy, E_T^{miss}**

1024 There exists several algorithms to reconstruct the E_T^{miss} at the HLT. The *missing H_T* ⁵
 1025 (*MHT*) algorithm calculates E_T^{miss} as the negative sum of transverse energy of calibrated
 1026 jets, constructed from calibrated topological clusters of calorimeter cells. This algorithm
 1027 is the most relevant to the analysis presented in Chapter 5. The *cell algorithm* is based
 1028 on the negative sum of transverse energy deposited in calorimeter cells above a certain
 1029 noise threshold. Unlike the cell algorithm, which calculates E_T^{miss} on the electromagnetic
 1030 scale, the MHT algorithm looks at jets calibrated using jet energy scale, so that numer-
 1031 ical threshold values for similar signal efficiencies differ. *Pufit*, a third algorithm, was
 1032 employed to disentangle calorimeter deposits from the hard-scatter, from those originat-
 1033 ing from pile-up interactions by grouping towers made out of topological clusters into
 1034 a pile-up and a hard-scatter category. This grouping is based on their energy, where the
 1035 threshold itself is dependent on the overall event activity measured by the total energy
 1036 deposited in the calorimeter. The assumption is that the contribution to E_T^{miss} due to pile-
 1037 up interactions is zero. Nevertheless a minimisation, which takes into account resolution
 1038 terms, determines an effective energy density from pile-up interaction which allows a
 1039 vanishing contribution to E_T^{miss} by the pile-up calorimeter towers. This correction is then
 1040 subtracted from the hard-scatter towers. The negative sum of transverse energy of those
 1041 pile-up corrected hard-scatter towers will provide the final E_T^{miss} value [43].

1042 Figure 3.9 shows the turn-on curves for various E_T^{miss} triggers: Figure 3.9a shows
 1043 the efficiency as a function of *modified*⁶ offline E_T^{miss} for three different E_T^{miss} trigger al-
 1044 gorithms, using early 2016 pp collision data. The events have been selected using single
 1045 lepton (electron or muon) triggers. The x-axis shows the offline E_T^{miss} calculated from
 1046 the sum of electrons, photons and jets, without the contributions from the muons. Three
 1047 different E_T^{miss} high-level trigger algorithms are shown: HLT_xe80_tc_lcw_L1XE50 cal-
 1048 culates E_T^{miss} based on calibrated clusters of calorimeter cells, and has a threshold of 80
 1049 GeV. HLT_xe90_mht_L1XE50 calculates E_T^{miss} based on reconstructed jets, and it has a
 1050 threshold of 90 GeV. HLT_xe100_L1XE50 calculates E_T^{miss} based on calorimeter cells cal-
 1051 brated at the electromagnetic scale, and has a threshold of 100 GeV. All three algorithms
 1052 are seeded by a Level-1 trigger algorithm with a threshold of 50 GeV which is also shown;
 1053 Figure 3.9b shows the combined L1 and HLT efficiency of the missing transverse energy
 1054 triggers HLT_xe110_pufit_L1XE50 and HLT_xe110_mht_L1XE50 as well as the efficiency
 1055 of the corresponding L1 trigger (L1_XE50) are shown as a function of the reconstructed
 1056 E_T^{miss} (*modified* to count muons as invisible) using pp collision data collected in 2017.
 1057 The events shown are taken from data with a $W \rightarrow \ell\nu$ selection to provide a sample en-
 1058 riched in real E_T^{miss} . The HLT E_T^{miss} of the *pufit* algorithm is calculated as the negative

⁵ H_T is the scalar sum of the various p_T s in the event, $H_T = \sum_i p_T^i$.

⁶ To calculate the E_T^{miss} efficiency, e. g. in events with muons, a muon trigger must be employed, therefore muon contributions are removed.

of the transverse momentum vector sum of all calorimeter topological clusters corrected for pileup. The pileup correction is done by grouping the clusters into coarser “towers” which are then marked as pileup if their E_T falls below a pileup-dependent threshold.

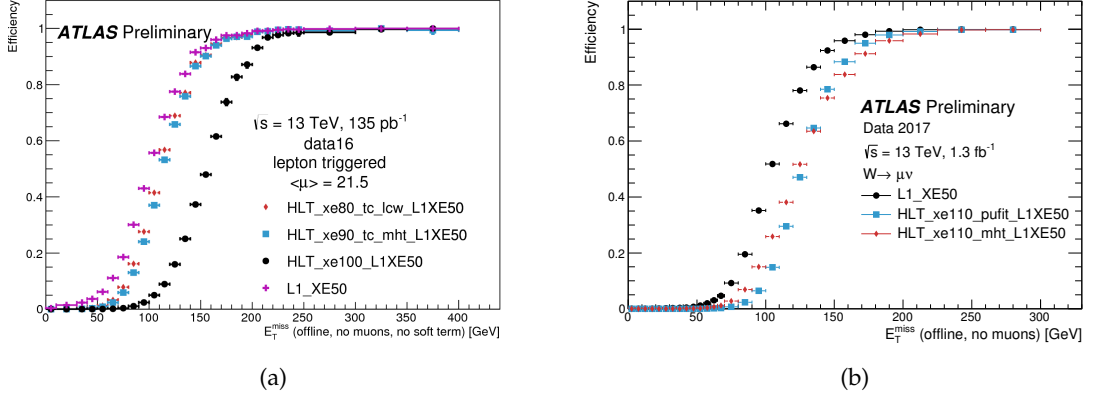


Figure 3.9: Turn-on curves of various E_T^{miss} triggers: Figure 3.9a shows the efficiency as a function of off-line E_T^{miss} for three different E_T^{miss} trigger algorithms. Three different E_T^{miss} high-level trigger algorithms are shown: HLT_xe80_tc_lcw_L1XE50 calculates E_T^{miss} based on calibrated clusters of calorimeter cells, and has a nominal threshold of 80 GeV. HLT_xe90_mht_L1XE50 calculates E_T^{miss} based on reconstructed jets, and has a nominal threshold of 90 GeV. HLT_xe100_L1XE50 calculates E_T^{miss} based on calorimeter cells calibrated at the electromagnetic scale, and has a nominal threshold (at the electromagnetic scale) of 100 GeV. All three algorithms are seeded by a Level-1 trigger algorithm with a nominal threshold of 50 GeV which is also shown; Figure 3.9b shows missing transverse energy trigger efficiencies for HLT_xe110_pufit_L1XE50 and HLT_xe110_mht_L1XE50 and for the corresponding L1 seed (L1_XE50). (from [7]).

1062 **4** | Event Simulation and Reconstruc-
1063 tion

1064 bla bla bla

1065 **4.1 Event Simulation**

1066 bla bla

1067 bla bla

1068 bla bla

1069 bla bla

1070 **4.1.1 Event Generation**

1071 bla bla bla

1072 bla bla bla

1073 bla bla bla

1074 bla bla bla

1075 **4.1.2 Detector Simulation**

1076 bla bla bla

1077 bla bla bla

1078 bla bla bla

1079 **4.2 Object Reconstruction**

1080 bla bla bla

1081 bla bla bla

1082 **4.2.1 Tracks and vertices**

1083 bla bla bla

1084 bla bla bla

1085 **4.2.2 Electrons**

1086 bla bla bla

1087 bla bla bla

1088 **4.2.3 Muons**

1089 bla bla bla

1090 bla bla bla

1091 **4.2.4 Jets**

1092 bla bla bla

1093 bla bla bla

1094 **4.2.5 Missing Transverse Energy**

1095 bla bla bla

1096 bla bla bla

1097 **4.2.6 Overlap Removal**

1098 bla bla bla

1099 bla bla bla

1100 5 | Stop searches in final states with
1101 jets and missing transverse en-
1102 ergy

1103 **6** | Results and Statistical Interpretations

1104

¹¹⁰⁵ **Appendix A**

1106 Bibliography

- 1107 [1] ATLAS Collaboration, “Summary plots from the atlas standard model physics
 1108 group.” <https://atlas.web.cern.ch/Atlas/GROUPS/PHYSICS/>
 1109 CombinedSummaryPlots/SM/ATLAS_a_SMSummary_TotalXsect/ATLAS_a_
 1110 SMSummary_TotalXsect.png. [viii](#), [9](#)
- 1111 [2] C. Borschensky, M. Krämer, A. Kulesza, M. Mangano, S. Padhi, T. Plehn, and
 1112 X. Portell, *Squark and gluino production cross sections in pp collisions at $\sqrt{s} = 13, 14, 33$*
 1113 *and 100 TeV*, *Eur. Phys. J.* **C74** no. 12, (2014) 3174, [arXiv:1407.5066](https://arxiv.org/abs/1407.5066) [hep-ph].
 1114 [viii](#), [16](#)
- 1115 [3] C. Lefèvre, *The CERN accelerator complex.,*
 1116 <http://cds.cern.ch/record/1260465>. [ix](#), [21](#), [22](#)
- 1117 [4] ATLAS Collaboration, *The ATLAS experiment at the CERN Large Hadron Collider*,
 1118 *Journal of Instrumentation* **3** no. 08, (2008) S08003.
 1119 <http://stacks.iop.org/1748-0221/3/i=08/a=S08003>. [ix](#), [23](#), [28](#), [31](#), [32](#)
- 1120 [5] A. Collaboration, *Performance of the ATLAS Trigger System in 2015*, *Eur. Phys. J.* **C77**
 1121 (2017), [arXiv:1611.09661](https://arxiv.org/abs/1611.09661) [hep-ex]. [ix](#), [31](#), [34](#), [36](#), [37](#), [38](#)
- 1122 [6] ATLAS Collaboration, *Performance of the ATLAS Trigger System in 2010*, *Eur. Phys. J.*
 1123 **C72** (2012), [arXiv:1110.1530](https://arxiv.org/abs/1110.1530) [hep-ex]. [ix](#), [31](#), [32](#), [33](#), [34](#)
- 1124 [7] ATLAS Collaboration, “Missing energy trigger public results.”
 1125 [https://twiki.cern.ch/twiki/bin/view/AtlasPublic/
 1126 MissingEtTriggerPublicResults](https://twiki.cern.ch/twiki/bin/view/AtlasPublic/MissingEtTriggerPublicResults). [x](#), [40](#)
- 1127 [8] M. Herrero, *The Standard Model.*, <https://arxiv.org/abs/hep-ph/9812242>.
 1128 [2](#)
- 1129 [9] ATLAS Collaboration, *Observation of a New Particle in the Search for the Standard*
 1130 *Model Higgs Boson with the ATLAS Detector at the LHC*, *Phys.Lett.* **B716** (2012),
 1131 [arXiv:1207.7214](https://arxiv.org/abs/1207.7214) [hep-ex]. [2](#)
- 1132 [10] CMS Collaboration, *Observation of a new boson at a mass of 125 GeV with the CMS*
 1133 *experiment at the LHC*, *Phys.Lett.* **B716** (2012), [arXiv:1207.7235](https://arxiv.org/abs/1207.7235) [hep-ex]. [2](#)

- 1134 [11] A. Pich, *The Standard Model of Electroweak Interactions*, [arXiv:1201.0537](https://arxiv.org/abs/1201.0537)
 1135 [hep-ph]. 4, 6
- 1136 [12] K. A. Olive at al. (Particle Data Group), *Review of Particle Physics*, [Chin.Phys. C](https://doi.org/10.1088/1674-113X/38/9/090001) **38**(9) (2014). 4
- 1138 [13] J. Goldstone, A. Salam and S. Weinberg, *Broken Symmetries*, [Phys. Rev.](https://doi.org/10.1103/PhysRev.127.965) **127** (1962) 965–970. 7
- 1140 [14] S. Weinberg, *Implications of Dynamical Symmetry Breaking*, [Phys. Rev.](https://doi.org/10.1103/PhysRevD.19.1277) **D19** (1976) 1277–1280. 9
- 1142 [15] Super-Kamiokande Collaboration, Y. Fukuda et al., *Evidence for oscillation of atmospheric neutrinos*, [Phys. Rev. Lett.](https://doi.org/10.1103/PhysRevLett.81.1562) **81** (1998) 1562–1567,
 1143 [arXiv:hep-ex/9807003](https://arxiv.org/abs/hep-ex/9807003) [hep-ex]. 9
- 1145 [16] SNO Collaboration, *Measurement of the Rate of $\nu_e + d \rightarrow p + p + e^-$ Interactions Produced by 8B Solar Neutrinos at the Sudbury Neutrino Observatory*, [Phys. Rev. Lett.](https://doi.org/10.1103/PhysRevLett.87.091301) **87** (2001). 9
- 1148 [17] T. O. W. of the Nobel Prize. https://www.nobelprize.org/nobel_prizes/physics/laureates/2015/. 9
- 1150 [18] F. Jegerlehner, *The hierarchy problem of the electroweak Standard Model revisited*,
 1151 [arXiv:1305.6652](https://arxiv.org/abs/1305.6652) [hep-ph]. 12
- 1152 [19] A. H. Chamseddine, R. Arnowitt, and P. Nath, *Locally Supersymmetric Grand
 1153 Unification*, [Phys. Rev. Lett.](https://doi.org/10.1103/PhysRevLett.49.970) **49** (1982) 970–974.
 1154 <https://link.aps.org/doi/10.1103/PhysRevLett.49.970>. 12
- 1155 [20] A. Arbey, M. Battaglia, A. Djouadi, F. Mahmoudi, and J. Quevillon, *Implications of a
 1156 125 GeV Higgs for supersymmetric models*, [Physics Letters B](https://doi.org/10.1016/j.physlettb.2012.01.030) **708** no. 1, (2012) 162 –
 1157 169. <http://www.sciencedirect.com/science/article/pii/S0370269312000810>. 12
- 1159 [21] L. Randall and R. Sundrum, *Out of this world supersymmetry breaking*, [Nucl. Phys.](https://doi.org/10.1016/S0550-3213(99)00356-7)
 1160 **B557** (1999) 79–118, [arXiv:hep-th/9810155](https://arxiv.org/abs/hep-th/9810155) [hep-th]. 12
- 1161 [22] G. F. Giudice, M. A. Luty, H. Murayama, and R. Rattazzi, *Gaugino mass without
 1162 singlets*, [JHEP](https://doi.org/10.1088/1126-6708-1998-12-027) **12** (1998) 027, [arXiv:hep-ph/9810442](https://arxiv.org/abs/hep-ph/9810442) [hep-ph]. 12
- 1163 [23] H. E. Haber and G. L. Kane, *The Search for Supersymmetry: Probing Physics Beyond the
 1164 Standard Model*, [Phys. Rept.](https://doi.org/10.1016/0370-1574(85)90055-7) **117** (1985) 75–263. 14
- 1165 [24] K. Hidaka and A. Bartl, *Impact of bosonic decays on the search for the lighter stop and
 1166 sbottom squarks*, [Phys. Lett.](https://doi.org/10.1016/S0370-2693(00)00202-1) **B501** (2001) 78–85, [arXiv:hep-ph/0012021](https://arxiv.org/abs/hep-ph/0012021)
 1167 [hep-ph]. 14

- 1168 [25] J.M. Jowett, M. Schaumann, R. Alemany, R. Bruce, M. Giovannozzi, P. Hermes, W.
 1169 Hofle, M. Lamont, T. Mertens, S. Redaelli, J. Uythoven, J. Wenninger, *The 2015*
 1170 *Heavy-Ion Run of the LHC*, [http://accelconf.web.cern.ch/accelconf/
 1171 ipac2016/papers/tupmw027.pdf](http://accelconf.web.cern.ch/accelconf/ipac2016/papers/tupmw027.pdf). 20
- 1172 [26] O. S. Brüuning, P. Collier, P. Lebrun, S. Myers, R. Ostojic, J. Poole and P. Proudlock,
 1173 *LHC Design Report*, <https://cds.cern.ch/record/782076>. 20, 21
- 1174 [27] CMS Collaboration, *The CMS experiment at the CERN LHC*, Journal of
 1175 Instrumentation **3** no. 08, (2008) S08004.
 1176 <http://stacks.iop.org/1748-0221/3/i=08/a=S08004>. 21
- 1177 [28] LHCb Collaboration, et. al, *The LHCb Detector at the LHC*, **JINST** (2008). 21
- 1178 [29] ALICE Collaboration, *The ALICE experiment at the CERN LHC*, Journal of
 1179 Instrumentation **3** no. 08, (2008) S08002.
 1180 <http://stacks.iop.org/1748-0221/3/i=08/a=S08002>. 21
- 1181 [30] A. Yamamoto, Y. Makida, R. Ruber, Y. Doi, T. Haruyama, F. Haug, H. ten Kate,
 1182 M. Kawai, T. Kondo, Y. Kondo, J. Metselaar, S. Mizumaki, G. Olesen, O. Pavlov,
 1183 S. Ravat, E. Sbrissa, K. Tanaka, T. Taylor, and H. Yamaoka, *The ATLAS central*
 1184 *solenoid*, **Nuclear Instruments and Methods in Physics Research Section A:**
 1185 *Accelerators, Spectrometers, Detectors and Associated Equipment* **584** no. 1, (2008)
 1186 **53 – 74**. [http://www.sciencedirect.com/science/article/pii/
 1187 S0168900207020414](http://www.sciencedirect.com/science/article/pii/S0168900207020414). 23
- 1188 [31] ATLAS Collaboration, *The ATLAS Inner Detector commissioning and calibration*, **Eur.**
 1189 **Phys. JC70**, arXiv:1004.5293. 24
- 1190 [32] ATLAS Collaboration, *ATLAS Insertable B-Layer Technical Design Report*,
 1191 <https://cds.cern.ch/record/1291633>. 25, 35
- 1192 [33] G. A. et al., *ATLAS pixel detector electronics and sensors*, Journal of Instrumentation **3**
 1193 no. 07, (2008) P07007.
 1194 <http://stacks.iop.org/1748-0221/3/i=07/a=P07007>. 25
- 1195 [34] A. Bingül, *The ATLAS TRT and its Performance at LHC*, Journal of Physics:
 1196 Conference Series **347** no. 1, (2012) 012025. [http://iopscience.iop.org/
 1197 article/10.1088/1742-6596/347/1/012025/meta](http://iopscience.iop.org/article/10.1088/1742-6596/347/1/012025/meta). 26
- 1198 [35] ATLAS Collaboration, *ATLAS liquid-argon calorimeter: Technical Design Report*,
 1199 <https://cds.cern.ch/record/331061>. 27
- 1200 [36] ATLAS Collaboration, *ATLAS muon spectrometer: Technical design report*,
 1201 <https://cds.cern.ch/record/331068>. 28

- 1202 [37] ATLAS Collaboration, *Fast TracKer (FTK) Technical Design Report,*.
 1203 <https://cds.cern.ch/record/1552953>. 29
- 1204 [38] E. Simoni, *The Topological Processor for the future ATLAS Level-1 Trigger: from design to*
 1205 *commissioning*, [arXiv:1406.4316](https://arxiv.org/abs/1406.4316). 31
- 1206 [39] R. Achenbach, P. Adragna, V. Andrei, P. Apostologlou, B. Åsman, C. Ay, B. M.
 1207 Barnett, B. Bauss, M. Bendel, C. Bohm, J. R. A. Booth, I. P. Brawn, P. B. Thomas,
 1208 D. G. Charlton, N. J. Collins, C. J. Curtis, A. Dahlhoff, A. O. Davis, S. Eckweiler, J. P.
 1209 Edwards, E. Eisenhandler, P. J. W. Faulkner, J. Fleckner, F. Föhlisch, J. Garvey,
 1210 C. N. P. Gee, A. R. Gillman, P. Hanke, R. P. Hatley, S. Hellman, A. Hidvégi, S. J.
 1211 Hillier, K. Jakobs, M. Johansen, E. E. Kluge, M. Landon, V. Lendermann, J. N. Lilley,
 1212 K. Mahboubi, G. Mahout, A. Mass, K. Meier, T. Moa, E. Moyse, F. Müller,
 1213 A. Neusiedl, C. Nöding, B. Oltmann, J. M. Pentney, V. J. O. Perera, U. Pfeiffer,
 1214 D. P. F. Prieur, W. Qian, D. L. Rees, S. Rieke, F. Rühr, D. P. C. Sankey, U. Schäfer,
 1215 K. Schmitt, H. C. Schultz-Coulon, C. Schumacher, S. Silverstein, R. J. Staley,
 1216 R. Stamen, M. C. Stockton, S. Tapprogge, J. P. Thomas, T. Trefzger, P. M. Watkins,
 1217 A. Watson, P. Weber, and E. E. Woehrling, *The ATLAS Level-1 Calorimeter Trigger*,
 1218 Journal of Instrumentation 3 no. 03, (2008) P03001.
 1219 <http://stacks.iop.org/1748-0221/3/i=03/a=P03001>. 32
- 1220 [40] ATLAS Collaboration, *Expected Performance of the ATLAS Experiment - Detector,*
 1221 *Trigger and Physics*, [arXiv:0901.0512 \[hep-ex\]](https://arxiv.org/abs/0901.0512). 33
- 1222 [41] ATLAS Collaboration, F. Miano, *The design and performance of the ATLAS Inner*
 1223 *Detector trigger for Run 2 LHC collisions at $\sqrt{s} = 13 \text{ TeV}$* , PoS **ICHEP2016** (2016) 856.
 1224 35
- 1225 [42] ATLAS Collaboration Collaboration, *Performance of primary vertex reconstruction in*
 1226 *proton-proton collisions at $\sqrt{s} = 7 \text{ TeV}$ in the ATLAS experiment*, Tech. Rep.
 1227 ATLAS-CONF-2010-069, CERN, Geneva, Jul, 2010.
 1228 [http://cds.cern.ch/record/1281344](https://cds.cern.ch/record/1281344). 37
- 1229 [43] N. Ruthmann, Y. Nakahama, and C. Leonidopoulos, *Trigger Menu in 2016*, Tech.
 1230 Rep. ATL-COM-DAQ-2016-137, CERN, Geneva, Sep, 2016.
 1231 <https://cds.cern.ch/record/2216366>. 39